Search for Charged Higgs Bosons at LEP in General Two Higgs Doublet Models

M. Battaglia[1], M. Ellert[2], T. Ekelof[2], G. Gómez-Ceballos[3], A. Kiiskinen[4], P. Lutz[5] and F. Matorras[3]

[1]CERN, Geneva, Switzerland

[2]Uppsala University, Uppsala, Sweden

[3]Universidad de Cantabria, Santander, Spain

[4]Helsinki Institute of Physics, Helsinki, Finland

[5]CEA, Saclay, France

Abstract

A search for pair-produced charged Higgs bosons was performed in the data collected by the DELPHI detector at LEP II at centre-of-mass energies from 189 GeV to 209 GeV. Five different final states, $\tau^+\nu_\tau\tau^-\bar{\nu}_\tau$, $c\bar{s}\bar{c}s$, $c\bar{s}\tau^-\bar{\nu}_\tau$, W*AW*A and W*A$\tau^-\bar{\nu}_\tau$ were considered, accounting for the major expected decays in type I and type II Two Higgs Doublet Models. No significant excess of data compared to the expected Standard Model processes was observed. The existence of a charged Higgs boson with mass lower than 76.7 GeV/c^2 (type I) or 74.4 GeV/c^2 (type II) is excluded at the 95% confidence level, for a wide range of the model parameters. Model independent cross-section limits have also been calculated.

Contributed Paper for ICHEP 2004 (Beijing)

1 Introduction

A search for pair-produced charged Higgs bosons in e^+e^- collisions was performed using the data collected by DELPHI during the LEP runs at centre-of-mass energies from 189 GeV to 209 GeV. The results reported here supersede those obtained in an earlier analysis of the DELPHI data [1]. Similar searches have been performed by the other LEP experiments [2].

The existence of a pair of charged Higgs bosons is predicted by several extensions of the Standard Model. Pair-production of charged Higgs bosons occurs mainly via s-channel exchange of a photon or a Z^0 boson. In Two Higgs Doublet Models (2HDM), the couplings are completely specified in terms of the electric charge and the weak mixing angle, θ_W, and therefore the production cross-section depends only on the charged Higgs boson mass. Higgs bosons couple to mass and therefore decay preferentially to heavy particles, but the precise branching ratios may vary significantly depending on the model. In most cases, for the masses accessible at LEP energies, the $\tau^-\bar{\nu}_\tau$ and $\bar{c}s$ decay[1] channels are expected to dominate. This is the case of the so-called type II 2HDM Models [3], where one Higgs doublet couples only to up-type fermions and the other to down-type fermions. Analyses of the three possible final states, $\tau^+\nu_\tau\tau^-\bar{\nu}_\tau$, $c\bar{s}\bar{c}s$ and $c\bar{s}\tau^-\bar{\nu}_\tau$, have been performed and are described in this paper. To avoid loss of generality, the results are combined and interpreted treating the Higgs decay branching fraction to leptons as a free parameter. An alternative set of models, type I models [4], assume that all fermions couple to the same Higgs doublet. In this case and if the neutral pseudo-scalar A is light (which is not excluded by direct searches for general 2HDM [5]) the decay to W^*A can be predominant even in the range of masses of interest at LEP (W^* is an off-shell W boson). Figs. 1 and 2 show the branching ratios for different parameters in type I models [6]. To cover the possibility of a light A boson the final states W^*AW^*A and $W^*A\tau^-\bar{\nu}_\tau$ were also looked for. The channel $W^*A\bar{c}s$ is not considered because its contribution is expected to be small. Type I models are explored through the combination of all the five channels, with or without W^*A decays. The combination is performed according to the branching ratios predicted by the model as a function of the ratio of the Higgs vacuum expectation ($\tan\beta$) and the boson masses.

Previous studies [7] exclude masses below 43.5 GeV/c^2, for type II models. The limit is also valid for type I models when the W^*A decay is not kinematically allowed or its branching ratio is small. Electroweak precision measurements [8] set indirect bounds on the charged Higgs mass regardless of its decay branching ratios. The tree-level decay amplitude $\Gamma(Z^0 \rightarrow H^+H^-)$ is independent of the model assumptions and can be calculated within 2HDM to be[9]

$$\Gamma(Z^0 \rightarrow H^+H^-) = \frac{G_F{M_Z}^3}{6\sqrt{2}\pi}\left(\frac{1}{2} - \sin^2\theta_W\right)^2\left(1 - \frac{4M_H^2}{M_Z^2}\right)^{\frac{3}{2}}, \tag{1}$$

where G_F is the Fermi coupling constant, M_H and M_Z are the masses of the charged Higgs and Z^0 and $\sin\theta_W$ is the weak mixing angle. The difference between the measured decay width of the Z^0 (Γ_Z) and the prediction from the Standard Model sets a limit to any non-standard contribution to the Z^0 decay. The current results [8] set the limit $\Gamma_{nonSM} < 2.9$

---

[1]Here and in the following all the decay modes are referred to the H^-, the charge conjugated being in all cases considered.

MeV/c^2 at 95% C.L. (taking into account both experimental and theoretical errors), which combined with the above expression sets the limit M_H > 39.6 GeV/c^2 at 95% C.L. As a consequence, the searches in this analysis are performed for charged Higgs boson masses of 38 GeV/c^2 or larger. The limits described here are only valid if the neutral pseudoscalar is heavy enough to allow the $b\bar{b}$ decay.

Different techniques were developed to improve the discrimination against the dominant W^+W^- background using multidimensional estimators based on discriminant variables such as the boson production angle, jet flavour tagging or τ polarisation.

2   Data sample

Data collected during the 2000 LEP run at centre-of-mass energies from 200 GeV to 209 GeV were used, with a total integrated luminosity of about 220 pb^{-1}. The data were grouped into two samples with centre-of-mass energies above or below 205.5 GeV, respectively. In the following, the average energy is quoted for each of these two samples. Approximately 60 pb^{-1} of these data were collected when one of the sectors of the Time Projection Chamber (TPC) was not operational (referred to as the S6 period in the following). The data collected during the years 1998 and 1999 at centre-of-mass energies from 189 GeV to 202 GeV were reanalysed, to take advantage of the improved performance of the reconstruction and selection. The additional data amounted to approximately 380 pb^{-1}.

The DELPHI detector and its performance have already been described in detail elsewhere [10, 11].

The background estimates for the different Standard Model processes were based on the following event generators: KK2f [12] for $q\bar{q}(\gamma)$ and $\mu^+\mu^-(\gamma)$, KORALZ [13] for $\tau^+\tau^-(\gamma)$, BHWIDE [14] for $e^+e^-(\gamma)$ and WPHACT [15] for four-fermion final states. The four-fermion samples were complemented with two-photon interactions, generated with TWOGAM [16] for hadronic final states, DIAG36 [17] for electron final states and RADCOR [17] for other leptonic final states. The quark hadronisation was simulated with JETSET 7.4 [18] and comparisons were made with HERWIG [19] and ARIADNE [20]. All the relevant background were simulated at each of the main centre-of-mass energies with an equivalent luminosity of at least 40 times that recorded for the data.

Signal samples were simulated using the HZHA generator [21] for charged Higgs masses from 40 to 100 GeV/c^2 in steps of 10 GeV/c^2, with additional points at 75, 85 and 95 GeV/c^2. For decays involving a neutral pseudoscalar, its mass was varied from 20 GeV/c^2 up to the charged Higgs mass, with the same step width, with additional points at 12 GeV/c^2. 2000 events were simulated for each mass point for each of the five decay channels at the same centre-of-mass energies. W* and A bosons, if present, were allowed to decay according to the Standard Model and Two Higgs Doublet Model expectations, respectively.

A specific simulation, with the appropriate detector conditions, was performed for the S6 period, both for signal and for background.

3 Analysis

Most of the techniques and requirements follow closely those used for the selection of
W^+W^- pairs [22], since the topology of the H^+H^- signal is very similar. We briefly
describe them here together with other techniques specific to the present analyses.

3.1 Run selection and particle selection

To ensure a good detector performance the data corresponding to runs in which subde-
tectors relevant to the analysis were not fully operational were discarded. In particular
it was required that the tracking subdetectors and calorimeters were fully operational.
An exception for the S6 period was made, because the redundancy of the tracking sys-
tem of the DELPHI detector made possible the use of these data without a significant
degradation of the analyses. For all the topologies that involved leptons, it was further
required that the muon chambers were active. This resulted in slightly smaller integrated
luminosities than for the hadronic channel. Table 1 summarizes the luminosities selected
in each case at every centre-of-mass energy.

$\sqrt{s}$(GeV)	$\mathcal{L}$ (leptonic)	$\mathcal{L}$ (hadronic)
189	153.8	158.0
192	24.5	25.9
196	72.4	76.9
200	81.8	84.3
202	39.4	41.1
205	69.1	75.6
206.6	79.8	87.8
206.3(S6)	50.0	60.8

Table 1: Integrated luminosity in pb^{-1} selected for leptonic and hadronic final states at
the different centre-of-mass energies.

Only charged particle tracks with an impact parameter in the transverse plane[2] smaller
than 5 cm, and with an axial coordinate $|z| < 10$ cm at the point of closest approach
to the beam spot, were accepted. Those with a relative momentum error $\frac{\Delta p}{p} > 1$ were
rejected.

Showers in the calorimeters were accepted as neutral particles if their energy was above
200 MeV and they were not associated to a charged particle track.

3.2 Lepton identification

To perform lepton identification, an initial clustering of particles into jets was performed
with the LUCLUS [18] algorithm.

Jets containing only one charged particle and no neutral particles, which were isolated
by more than 15° from the remaining particles in the event were initially considered as

---

[2]The co-ordinate system used has the z-axis parallel to the electron beam, and the polar angle cal-
culated with respect to this axis. The plane perpendicular to the z axis will be called hereafter the
transverse plane.

lepton candidates. One of these isolated charged particles was identified as a muon if it gave signal in the muon chambers or left a signal in the calorimeters compatible with a minimum ionising particle (MIP). It was identified as an electron if its energy deposition in the electromagnetic calorimeters was compatible with its measured momentum and the ionisation loss in the TPC was compatible with that expected from an electron of that momentum.

If an electron or muon had a momentum and energy deposition in the electromagnetic calorimeters smaller than $0.13\sqrt{s}$, it was assumed to come from a τ decay and was therefore tagged as τ. In addition, isolated jets with an energy of at least 5 GeV, at least one and at most five charged particles and no more than ten particles in total were also considered as τ candidates.

When dealing with semileptonic final states, the τ candidate jet definition was refined removing particles that were not likely to come from a τ decay. Particles contained inside the jet, but forming an angle with the jet axis of more than $15°$ were removed from the jet. If the invariant mass of the jet was greater than 2.5 GeV/c^2, the particle giving the largest contribution to the mass (excluding the highest momentum charged particle in the jet) was excluded. This procedure was repeated until the mass no longer exceeded 2.5 GeV/c^2.

If more than one τ candidate was found they were sorted with the following order of precedence: muon, electron, narrowest jet (defined as the one whose momentum weighted angular spread was lowest), single charged particle. For purely leptonic events the first two candidates were retained and the rest were neglected as τ particles. For semileptonic events, only the first one was retained as a τ candidate.

In some of the analyses, the particular decay of the τ had to be identified. All τ candidates were classified into the following categories (corresponding to the major decay modes): e, μ, π, $\pi + n\gamma$, $\geq 3\pi$ according to the lepton identification, the number of charged particles of the jet and the number of photons.

3.3   Likelihood ratio technique

In several of the analyses the background discrimination was performed by using a likelihood ratio technique. Signal and background likelihood functions, $\mathcal{L}_s$ and $\mathcal{L}_b$, were defined as products of the probability density functions of the N discriminating variables, $\mathcal{L}_s = \prod_{i=1,N} s_i(x_i)$ and $\mathcal{L}_b = \prod_{i=1,N} b_i(x_i)$. For each of the measured values of the N discriminating variables, x_i, the values of the signal and background probability densities, $s_i(x_i)$ and $b_i(x_i)$, were determined using samples of simulated signal and background events. The final event likelihood ratio, for simplicity referred to as "likelihood" in the following, was computed as a normalised ratio of the signal and background likelihoods, $\mathcal{L}_s/(\mathcal{L}_s + \mathcal{L}_b)$.

3.4   Tau polarisation

One of the methods used to discriminate charged Higgs from W bosons is based on the different spin of these particles, the Higgs being a scalar and the W a vector boson. This spin can be inferred if the decay involves τ leptons.

Assuming that the ν_τ has a definite helicity, the polarisation (P_τ) of tau leptons originating from heavy boson decays is determined entirely by the properties of weak

interactions and the spin of the parent boson. The helicity configuration for the signal is $H^- \rightarrow \tau_R^- \bar{\nu}_{\tau R}$ ($H^+ \rightarrow \tau_L^+ \nu_{\tau L}$) and for the W^+W^- background it is $W^- \rightarrow \tau_L^- \bar{\nu}_{\tau R}$ ($W^+ \rightarrow \tau_R^+ \nu_{\tau L}$) resulting in $P_\tau^H = +1$ and $P_\tau^W = -1$.

The τ weak decay induces a dependence of the angular and momentum distributions on the polarisation. Once the τ decay channel was identified, the information on the τ polarisation was extracted from the observed kinematic distributions of its decay products, e.g. angles and momenta. These kinematic variables can always be combined [23] into a single estimator, defined for each decay channel, without loss of information. These estimators are equivalent to those used at the Z^0 peak for precision measurements [24]. For charged Higgs boson masses close to the threshold, the boost of the bosons is relatively small and the τ energies are similar to that of the τ's from Z^0 decays at rest (40–50 GeV).

To compare events in which the τ had different decay modes coherently , the identified decay mode and P_τ estimator were combined into a likelihood function. When two τ candidates were present in one event, the likelihood functions were defined for each of them and then multiplied, assuming independence of the two τ (which was true to a large extent, except for some small correlations due to detector effects).

3.5 Jet definition and flavour tagging

When the charged particle multiplicity was larger than 6, the particles were clustered into jets using the DURHAM[25] algorithm. When a τ had been identified, the particles assigned to its jet were excluded from this clustering and the remaining particles were forced into exactly two jets. Each of the two jets was required to have a minimum of four particles of which at least one had to be charged. For the purely hadronic events, the jet algorithm was forced to produce a maximum of four jets.

In the $c\bar{s}\bar{c}s$ and $c\bar{s}\tau^-\bar{\nu}_\tau$ decay channels all hadronic jets in the event originate from a c or s quark. In the hadronic background processes, such as $q\bar{q}$ and W^+W^- events, often the jets have a different quark flavour or originate from a gluon. Therefore a jet flavour tagging algorithm was used as a tool in the analyses of the $c\bar{s}\bar{c}s$ and $c\bar{s}\tau^-\bar{\nu}_\tau$ channels, which follows a similar technique to that used by DELPHI in a determination of $|V_{cs}|$ at LEP II [26].

This tagging was based on nine discriminating variables, combined in a likelihood function: three of them were related to identified leptons and hadron content of the jet, two depended on kinematical variables and four on the reconstructed secondary decay structure. The finite lifetime of c particles was exploited to distinguish between c and light quark jets, while the c mass and decay multiplicity were used to discriminate against b jets. Furthermore s and c jets could be distinguished from u and d jets by the presence of an identified energetic kaon. Charged hadrons were identified combining the Ring Imaging Cherenkov (RICH) and TPC dE/dx [27] measurements. The responses of the flavour tagging algorithm for the individual jets were further combined into an event $c\bar{s}\bar{c}s$ probability or into a di-jet $\bar{c}s$ (or $c\bar{s}$) probability which were then used in background suppression.

3.6 Mass reconstruction

The masses of the decaying bosons were reconstructed using a constrained fit [28] requiring energy and momentum conservation with known beam energy (4C fit). For the topologies

studied in this analysis, the event had to be compatible with the hypothesis that the different objects were produced in the decay of two equal mass particles, so an additional constraint was applied requiring that the two mass combinations were equal (5C fit). These fits also provide the best estimation of the boson momenta.

In the case of channels involving a $\tau^-\bar{\nu}_\tau$ decay, the three components of the momentum vector of the ν_τ and the magnitude of the τ momentum were treated as unknown parameters, reducing the number of degrees of freedom of the fit from five to one. This fit also provided a good estimation of the τ 4-momentum.

In the $\tau^+\nu_\tau\tau^-\bar{\nu}_\tau$ final state, the number of unknowns was higher than the number of constraints and no mass could be estimated.

4   Selection

4.1   The $\tau^+\nu_\tau\tau^-\bar{\nu}_\tau$ channel

The signature for $H^+H^- \rightarrow \tau^+\nu_\tau\tau^-\bar{\nu}_\tau$ is large missing energy and momentum and two acollinear and acoplanar[3] τ jets containing either a lepton or one or a few hadrons. The main backgrounds are the W^+W^- leptonic decays, mainly those in which one W or both decayed to $\tau\nu$. Less important, but still not negligible, are the radiative $\tau^+\tau^-$ and two-photon events.

4.1.1   Event preselection

To select leptonic events a total charged particle multiplicity between 2 and 6 was required. Only events with two jets both containing at least one charged particle were retained. Events were rejected if both jets had more than one charged particle. It was also required that the angle between the two jets was larger than $30°$.

Two-fermion and two-photon events were rejected by requiring the acoplanarity to be larger than $13°$ if both jets were in the barrel region ($43° < \theta < 137°$) or larger than $25°$ otherwise.

The two-photon background was further reduced by different requirements on the jets: the sum of the jet energies transverse to the beam direction, $E_\perp$, was required to be greater than $0.1\sqrt{s}$; the total transverse momentum, P_T, to be greater than $0.04\sqrt{s}$; the total energy detected within $30°$ around the beam axis to be less than $0.1\sqrt{s}$; and the total energy outside this region to be greater than $0.1\sqrt{s}$.

To reject W^+W^- events where neither W decayed to $\tau\nu$, it was required that the two jets were identified as τ leptons.

4.1.2   Final background discrimination

Following the selection above most of the remaining background is $W^+W^- \rightarrow \tau^+\nu_\tau\tau^-\bar{\nu}_\tau$ events. The H^+H^- signal and the W^+W^- background have similar topologies and the presence of missing neutrinos in the decay of each of the bosons makes the boson mass reconstruction impossible. However, the boson polar angle distribution and the τ polarisation are different, providing means to discriminate between the two processes.

---

[3]The acoplanarity is defined as the supplement of the angle between the two jets projected onto the plane perpendicular to the beam.

A likelihood function was built to separate the signal from the background. It was composed of five variables: the τ polarisation likelihood of the event, the signed cosine of the polar angle [4] of both τ's (which carries information of the boson polar angle), the acoplanarity and the total transverse momentum. The first three variables discriminated between $\tau^+\nu_\tau\tau^-\bar{\nu}_\tau$ produced from W boson and charged Higgs pairs. The last two variables had some sensitivity to the boson mass and helped in the discrimination of the remaining background from other processes. Some of these variables are shown in Fig. 3 and the resulting likelihood distribution for data, expected backgrounds and signal is shown in Fig. 4. The effects of the different sets of cuts are shown in Table 2 for the combined 189–209 GeV sample.

cut	data	total bkg.	4-fermion	other bkg.	ε_{80}
Leptonic selection	175699	176685	921	175764	72.2%
Acoplanarity cut	16607	16576	715	15861	62.3%
Energy/momentum cuts	527	566.9	534.4	32.5	46.7%
τ identification	59	68.9	58.3	10.6	35.1%

Table 2: The total number of events observed and expected backgrounds in the $\tau^+\nu_\tau\tau^-\bar{\nu}_\tau$ channel after the different cuts used in the analysis at $\sqrt{s} = 189$–209 GeV. The last column shows the efficiency for a charged Higgs boson signal with $M_H = 80$ GeV/c^2.

4.2 The c$\bar{s}$$\bar{c}$s channel

In the analysis of the c$\bar{s}$$\bar{c}$s channel both charged Higgs bosons were assumed to decay into a pair of c and s quarks producing a final state with four jets. The two dominant background sources are the q$\bar{q}$ production with gluon radiation (q$\bar{q}gg$) and fully hadronic four-fermion final states. The four-fermion background from W$^+$W$^-$ production is much more severe than that from Z^{0}Z^0, because of the higher cross-section. In addition, the discriminant variables used against the W$^+$W$^-$ background usually work with similar performance against the Z^{0}Z^0 background. Therefore, the four-fermion sample is referred to as W$^+$W$^-$ in the remainder of the section.

4.2.1 Event preselection

In order to preselect hadronic events the following cuts were applied: the events had to contain at least 10 charged particles, the visible energy of the reconstructed particles, had to be larger than $0.6\sqrt{s}$, the reconstructed effective centre-of-mass energy[5], $\sqrt{s'}$, had to be larger than $0.85\sqrt{s}$. To reject hadronic back-to-back two-jet q$\bar{q}$ events the thrust was required to be less than 0.95.

To select only genuine four-jet events it was required that the DURHAM clustering distance for the transition from four to three jets, $y_{4\to3}$, was greater than 0.002 and each jet was required to have a mass larger than 2 GeV/c^2 and at least three particles, out of

---

[4]The signed cosine is defined as the charge of the particle multiplied by the cosine of its polar angle.

[5]The effective centre-of-mass energy was estimated from a three-constraint kinematic fit in order to test the presence of an initial state radiated photon lost in the beam pipe [29].

which at least two were charged. All jets were required to have a total energy above 5 GeV, and the minimum angle between any two jets was required to be at least 25°.

In order to obtain the best possible mass resolution a 5C fit was performed for each of the three possible di-jet combinations and the combination giving the smallest χ^2 was selected. A 4C fit was also performed for that di-jet combination, imposing only energy-momentum conservation, to estimate the difference between the masses of the two reconstructed bosons. As the uncertainty of the di-jet mass reconstruction is approximately proportional to the mass, the boson mass difference was renormalised dividing it by the mass provided by the 5C fit. In such a way, the resulting discriminant variable had less dependence on the signal mass. This relative mass difference of the two reconstructed bosons was required to be below 25%.

4.2.2 Final background discrimination

Significant amounts of $q\bar{q}gg$ background still remained after the preselection. To suppress it further an anti-$q\bar{q}$ likelihood function based on five variables was constructed as follows.

The first variable, the event aplanarity, exploits the differences in the event shape between signal and background. The second one, the cosine of the polar angle of the thrust axis, uses the fact that the signal events have a polar angle distribution with an approximate dependence as $\sin^2\theta$, whereas the jets in the $q\bar{q}$ background events are concentrated closer to the beam axis. The third variable was based on the product of the minimum angle between two jets and the minimum jet energy in the event and exploited the particular dependence of the probability of hard gluon radiation with the gluon energy and emission angle. The minimum energy and the minimum angle between jets are significantly different in signal events with low and high mass due to the large boost of light Higgs bosons. In order to reduce the mass dependence of the likelihood variable, the product was scaled dividing it by the reconstructed Higgs boson mass of the event. The fourth variable used the fact that the charged Higgs bosons have equal mass whereas the masses of the di-jet pairs in the $q\bar{q}$ events are more or less randomly distributed. Therefore the relative mass difference was a powerful discriminant variable. The last variable was the output of the event $c\bar{s}\bar{c}s$-tag described in Section 3.5. The normalised likelihood was required to exceed 0.4 to reject most of the $q\bar{q}$ background with a moderate signal efficiency loss (Table 3). Some of these variables are shown in Fig. 5.

Most of the background remaining after the anti-$q\bar{q}$ cut was hadronic decays of W pairs. If the mass of the charged Higgs boson coincides with the mass of the W boson the W^+W^- background is partly irreducible. Some differences, however, exist and were combined into an anti-WW likelihood in order to discriminate between these two processes.

The first of the variables in the anti-WW likelihood exploited the different polar angle distributions of the Higgs boson and the W boson, due to their different spins. This variable was the cosine of the polar angle of the positive boson, estimated assuming equal and opposite boson momenta. The charge was derived from the sum of the momentum weighted charges of the two jets [30] used to reconstruct the boson. The boson with the higher value of charge was assumed to be the positive one and the other was assumed to be the negative one. The second variable used for W^+W^- background discrimination was the $c\bar{s}\bar{c}s$ event tag output which is useful as all signal jets originate from c and s quarks and only half of the background jets have the same quark flavours. The last variable used was the relative mass difference between the two reconstructed bosons. This variable

8

has rejection power especially in cases where the reconstructed mass in W events is far away from the nominal W mass since in these events something has gone wrong in the jet momentum measurement, which usually leads to a higher mass difference between the reconstructed bosons. It also rejects more W^+W^- background than charged Higgs signal due to a larger natural width of the W boson. All events with anti-WW likelihood value below 0.3 were rejected.

The effects of the different sets of cuts are shown in Table 3 for the combined 189–209 GeV sample. The distribution of the anti-$q\bar{q}$ and anti-WW likelihoods at the preselection level are shown in Fig. 6. The reconstructed 5C fit mass distribution for data, expected backgrounds and signal after the anti-$q\bar{q}$ and anti-WW cuts is shown in Fig. 7 with the likelihood cut tightened to $\mathcal{L}_{qq} > 0.7$ and $\mathcal{L}_{WW} > 0.5$ to visually enhance the mass distribution of the events whose variables are closer to those expected for the charged Higgs signal.

cut	data	total bkg.	4-fermion	other bkg.	ε_{75}	ε_{80}
4-jet presel.	5890	5902.5	4076.9	1825.6	83.0%	84.1%
Mass diff.	4326	4354.2	3389.6	964.6	71.0%	71.8%
anti-$q\bar{q}$	2785	2808.1	2506.2	301.9	56.9%	57.8%
anti-WW	2114	2115.6	1855.5	260.1	52.8%	53.6%

Table 3: The total number of events observed and expected backgrounds in the $c\bar{s}\bar{c}s$ channel after the different cuts used in the analysis at $\sqrt{s}$ = 189–209 GeV. The last columns show the efficiencies for charged Higgs boson signals with $M_H = 75$ GeV/c^2 and $M_H = 80$ GeV/c^2, respectively.

4.3 The $c\bar{s}\tau^-\bar{\nu}_\tau$ channel

In the $c\bar{s}\tau^-\bar{\nu}_\tau$ channel one of the charged Higgs bosons decays into a $c\bar{s}$ quark pair, while the other decays into $\tau^-\bar{\nu}_\tau$. Such an event is characterised by two hadronic jets, a τ candidate and missing energy carried by the neutrinos. The dominating background processes are $q\bar{q}g(\gamma)$ events and semileptonic decays of W^+W^-.

4.3.1 Event preselection

An initial set of cuts was applied to reject purely leptonic events as well as two-photon interactions. The charged particle multiplicity had to be at least 6 and the total momentum of the charged particles had to be greater than $0.01\sqrt{s}$. The quantity $E_{fw} = \sqrt{E_{45}^2 + E_{135}^2}$, where E_{45} and E_{135} are the energies deposited in the electromagnetic calorimeters at $\theta < 45°$ and $\theta > 135°$ respectively, had to be less than $0.45\sqrt{s}$. The absolute value of the cosine of the polar angle of the missing momentum had to be less than 0.985 and the total transverse energy had to be greater than $0.2\sqrt{s}$. The electromagnetic energy within a 15° cone around the beam-pipe was required to be less than 30 GeV.

To remove $q\bar{q}\ell^+\ell^-$ four-fermion topologies, events with two or more leptons of the same flavour with momentum greater than $0.05\sqrt{s}$ and more than 10° isolation angle were rejected.

Another set of cuts was applied to reject the bulk of the $q\bar{q}\gamma$ radiative events. The absolute value of the cosine of the polar angle of the missing momentum had to be less than 0.96, the difference between the centre-of-mass energy and the effective centre-of-mass energy ($\sqrt{s}-\sqrt{s'}$) had to be greater than 10 GeV, the visible energy had to be lower than $0.85\sqrt{s}$. The DURHAM clustering distance $y_{4\to3}$ had to be less than 0.03. The angle between the most energetic neutral particle in the event and the missing momentum had to be greater than 25°. If the absolute value of the cosine of the polar angle of the missing momentum was greater than 0.8, the effective centre-of-mass energy ($\sqrt{s'}$) had to be greater than 105 GeV and its difference from the nominal centre-of-mass energy ($\sqrt{s}-\sqrt{s'}$) had to be greater than 25 GeV.

Background from W$^+$W$^-$ semileptonic decays not involving τ particles as well as a large fraction of the remaining $q\bar{q}$ background was rejected by requiring the presence of an identified τ. The momentum of the τ jet had to be greater than 5 GeV/c and the product of the τ candidate momentum and its isolation angle had to be larger than 150 GeV·degree. If the τ candidate jet contained more than one charged particle, the cone around its axis containing 75% of the jet energy had to be smaller than 10°.

Finally, if the 5C mass fit did not converge the event was rejected. This reduced the background from misreconstructed W$^+$W$^-$ pairs, with badly defined jets or with wrong pairing, contributing to masses very different from the expected W peak.

4.3.2 Final background discrimination

At this level of the selection there was still a very significant contribution of $q\bar{q}$ events. To reduce this background further a likelihood function was defined with eleven variables: the event thrust, the cosine of the missing momentum, the angle in the transverse plane between the two hadronic jets, the reconstructed polar angle of the negatively charged boson (with the charge defined according to that of the τ), the angle between the τ jet and the parent boson's momentum in the boson's rest-frame, the τ decay channel, the total transverse momentum, $\sqrt{s'}/\sqrt{s}$, the τ isolation, the DURHAM clustering distance $y_{3\to2}$ when going from three to two jets and the angle between the plane spanned by the two hadronic jets and the τ candidate. This angle took into account the fact that in most cases the $q\bar{q}$ background, produced when a radiated gluon was confused with a τ jet, tended to have all three jets in the same plane, while for the signal the τ is more or less uniformly distributed in space. Some of these variables are shown in Fig. 8 (a-c) and the likelihood is shown in Fig. 9 (top). Events with an anti-$q\bar{q}$ likelihood lower than 0.5 were rejected.

At this stage, most of the remaining background was W$^+$W$^-$ decaying to $q\bar{q}\tau^-\bar{\nu}_\tau$, whose topology is equivalent to that of the signal. Further background rejection was possible, however, using the τ polarisation and the output of the jet flavour algorithm. Another likelihood function was therefore defined using these two variables and some of the variables used in the previous anti-$q\bar{q}$ likelihood since these also improved the W$^+$W$^-$ rejection. The additional variables were the thrust, angle in the transverse plane between the two hadronic jets, the reconstructed polar angle of the negatively charged boson, the angle between the τ momentum and its parent boson's momentum in the boson's rest-frame and the τ isolation angle. Some of these variables are shown in Fig. 8 (d-f) and the result of the likelihood is shown in Fig. 9 (bottom). No cut was imposed on this function, but it was used in the limit estimation as described below. However,

10

Fig. 10, shows the mass distribution after a cut on $\mathcal{L}_{WW} > 0.5$ to visually enhance the mass distribution of the events whose variables are closer to those expected for the charged Higgs signal. The effects of the different sets of cuts are shown in Table 4 for the combined 189–209 GeV sample. At preselection level the background from two-photon events was slightly underestimated, due to the phase space cuts used in the generator. Further cuts in the analysis are tighter than those in the generation and therefore the background estimation is not affected.

cut	data	total bkg.	4-fermion	other bkg.	ε_{75}
Preselection	31138	29803.1	9449.0	20354.1	95.8%
Bulk q$\bar{\text{q}}$ rejection	6267	5899.7	3939.7	1960.0	84.9%
$qq\tau\nu$ selection	3054	2814.5	1649.0	1165.4	66.1%
anti-q$\bar{\text{q}}$ likelihood > 0.5	1085	1081.7	985.3	95.9	57.5%

Table 4: The number of events selected in the data and expected from Monte Carlo after the different cuts in the $c\bar{s}\tau^-\bar{\nu}_\tau$ analysis at $\sqrt{s} = 189$–209 GeV. The efficiency in the last column corresponds to a charged Higgs boson with a mass of 75 GeV/c^2.

4.4 Channels including a W$^*A$ decay

If at least one of the Higgs bosons decays to a W$^*A$ pair, there are several possible topologies depending on the different boson decays. The W can decay leptonically or hadronically, and the number of jets strongly depends on the A mass and on the boson boosts. The search was restricted to A masses above 12 GeV/c^2, where it decays predominantly to b$\bar{\text{b}}$ and an inclusive search was performed. Events with jets with b quark content were searched for in two topologies:

- events with a τ, missing energy and at least two hadronic jets

- events with no missing energy and at least four hadronic jets

In this way most of the possible decay chains for the W$^*A\tau^-\bar{\nu}_\tau$ (first topology) and W*AW*A (second) were covered. The decay to W*A$\bar{\text{c}}$s was neglected because its contribution is small. Its branching ratio is usually very small and only reaches a maximum of about 17% in a small region of the parameter space. In this region the branching ratio for W$^*A\tau^-\bar{\nu}_\tau$ is about twice as large, with a smaller background. The branching ratio for W*AW*A is about 30%, giving a signal almost indistinguishable from W*A$\bar{\text{c}}$s.

The analysis designed by DELPHI for technipion search within Technicolor models [32] was well suited also for these topologies and had a good performance in this search. It was therefore adopted here. A brief description of that analysis is outlined here.

4.4.1 Semileptonic final states.

Since the topology searched for in the semileptonic case is very close to the corresponding channel in W$^+$W$^-$ production, a selection similar to that used on W$^+$W$^-$ cross-section and decay branching ratio measurements [22] was applied at the first step. However,

variables strongly correlated with the boson mass were not used, making the analysis efficient for a wide range of masses.

Firstly loose initial cuts, requiring at least seven charged particles, transverse energy greater than $0.25\sqrt{s}$, less than 30 GeV in a 30° cone around the beam, and the polar angle of the missing momentum fulfilling $|\cos\theta_{miss}| < 0.985$, were used to remove a large fraction of the leptonic, $q\bar{q}(\gamma)$ and $\gamma\gamma$ events.

Then, an isolated τ candidate had to be found, to reduce the background from W^+W^- leptonic decays not involving τ particles. The isolation criterion was defined in terms of the product $p \cdot \theta_{iso}$, where p is the τ jet momentum and θ_{iso} is the isolation angle between the lepton and the nearest charged particle with momentum greater than 1 GeV/c.

To reject non-W^+W^- events, a neural network (NN) with the following variables was used: the jet momentum, isolation angle, cosine of the polar angle of the missing momentum, transverse momentum, thrust, angle between the lepton and the hadronic system, the acoplanarity and acollinearity of the hadronic jets and $\sqrt{s'/s}$. Events were accepted if the NN output was above 0.6. In this way most of the non-W^+W^- background is rejected.

The second step exploits the specific properties of the signal, such as the presence of b-quarks or the production angle, to distinguish it from the W pairs. This is done using another neural network which uses four input variables: the b-tagging variables of the two hadronic jets, the signed cosine of the polar angle of the boson[6] and $|\cos\theta_{miss}|$.

The effects of the different sets of cuts are shown in Table 5 for the combined 189–209 GeV sample. Fig. 12 (top) shows the reconstructed mass, using a 5C fit, of the selected candidates.

cut	data	total bkg.	4-fermion	other bkg.	$\varepsilon_{80/30}$
Hadronic preselection	28380	28274.8	3925.9	24348.9	88.9%
$q\bar{q}\tau\nu$ selection	1043	1061.9	884.5	177.4	44.0%
NN output > 0.1	39	36.8	22.2	14.6	22.6%
NN output > 0.2	18	17.8	7.9	9.9	17.9%
NN output > 0.3	12	11.0	3.7	7.3	14.9%

Table 5: The total number of events observed and expected backgrounds in the $W^*A\tau^-\bar{\nu}_\tau$ channel after the different cuts used in the analysis at $\sqrt{s}$ = 189–209 GeV. The last column shows the efficiencies for charged Higgs boson signals with $M_H = 80$ GeV/c^2 and M_A= 30 GeV/c^2.

4.4.2 Hadronic final states.

The W^*AW^*A analysis starts with the four-jet preselection used in the search for neutral Higgs bosons [33], which aims to eliminate the radiative and $\gamma\gamma$ events and to reduce the QCD and $Z^0\gamma^*$ background. The $q\bar{q}(\gamma)$ and 4-fermion backgrounds remaining after the preselection have to be reduced further. For this purpose different shape and b-tagging variables have been investigated. Finally, 12 variables were selected for this analysis and

---

[6]The sign is defined by the charge of the τ, and the production polar angle θ_{prod} is the one obtained from the 5C fit.

the final discriminant variable is defined as the output of a neural network. There were two b-tagging variables intended to reduce the W^+W^- background: one of them (x_b) is computed as the sum of the two highest jet b-tagging variables [31], and the other is the sum of the four jet b-tagging variables. Seven shape variables are used to reduce the $q\bar{q}(\gamma)$ contamination. They are the sum of the second and fourth Fox-Wolfram moments, the product of the minimum jet energy and the minimum opening angle between any two jets, the event thrust, the sum of the four lowest angles between any pair of jets in the event, the minimal di-jet mass, and the minimal y_{cut} values for which the event is clustered into 4 jets ($y_{4\rightarrow3}$) and into 5 jets ($y_{5\rightarrow4}$). Finally, three more variables take into account the two-boson event topology. To define them the event is forced into four jets, a five constraint fit requiring conservation of energy and momentum and equal masses of opposite jet pairs is applied to all possible jet pairings, and the pairing giving the smallest value of the fit χ^2 is selected. The variables then included in the neural network are the smallest χ^2, the production angle of the jet pair, and the angle between the planes defined by the two jet pairs.

The effects of the different sets of cuts are shown in Table 6 for the combined 189–209 GeV sample. Fig. 12 (bottom) shows the reconstructed mass, using a 5C fit, of the selected candidates.

cut	data	total bkg.	$q\bar{q}g$	4-fermion	$\varepsilon_{80/30}$
preselection	6592	6520.1	2004.9	4515.2	67.9%
NN output > 0.1	254	252.5	87.2	165.3	46.1%
NN output > 0.3	86	78.9	25.2	53.7	28.3%

Table 6: The total number of events observed and expected backgrounds in the W^*AW^*A channel after the different cuts used in the analysis at $\sqrt{s}$ = 189–209 GeV. The last column shows the efficiencies for charged Higgs boson signals with M_H = 80 GeV/c^2 and M_A= 30 GeV/c^2.

5   Systematic errors

Uncertainties in the expected background rates and in the signal efficiency were accounted for at each centre-of-mass energy and separately for the S6 period. Small contributions to the background rate uncertainties, of the order of 0.6%, are due to uncertainties in the luminosity measurement and in the theoretical cross-section estimates for the simulated data samples. The systematic error estimation for the background follows closely the treatment in the DELPHI W^+W^- cross-section measurement [22].

The largest part of the background and signal efficiency uncertainties in the $\tau^+\nu_\tau\tau^-\bar{\nu}_\tau$ channel is due to the limited simulation statistics available. The typical contribution was 8% and 1.5% respectively. Several additional sources of systematic uncertainties were investigated. In particular, the track reconstruction efficiency, the τ identification and the behaviour of different variables were studied.

The systematic errors induced by the track reconstruction and τ identification were checked by a comparison with independent samples of di-lepton or two-photon leptonic events of simulation and real data, taken with the same detector conditions both at high

energy and at the Z^0 resonance. These samples were selected by kinematic cuts, with only very loose particle identification requirements, which were found to be uncorrelated to those used in this analysis. The lepton identification efficiency estimation from data and simulation was found to agree within the statistical errors (about 1%). The same leptonic samples were used to check the track reconstruction efficiency of isolated particles, showing an agreement at the 1% level. The modelling of the preselection variables agrees within statistical errors with the data. The momentum and electromagnetic energy scales and resolutions were investigated using radiative di-lepton events, $\mu^+\mu^-\gamma$ or $e^+e^-\gamma$, from data and simulation. For these events, the momenta of the particles can be calculated with very good precision from kinematical constraints, independently of the direct measurement on the tracking detectors or calorimeters, allowing comparisons. In all cases, data and simulation agreed to better than the statistical precision, which had a negligible influence both in signal efficiency and background rates. Additional systematic effects were estimated by comparing the data collected at the Z^0 peak during the period when sector 6 of the TPC was not functioning with simulation samples produced with the same detector conditions. This did not indicate any significant increase in the systematic errors, compared to those quoted above. The total systematic error on the signal efficiency was 2% and the total relative systematic error on the background rate was 10%.

In the $c\bar{s}\bar{c}s$ analysis, the total uncertainty of the $q\bar{q}gg$ background estimate at the four-jet preselection level was dominated [22] by the hadronisation model and imperfections in the generator model. Based on a comparison of three models provided by the generators JETSET 7.4 [18], HERWIG [19] and ARIADNE [20], the total uncertainty of the $q\bar{q}gg$ event rate was estimated to be of the order of 5%.

Another uncertainty in four-fermion background (mainly W^+W^-), is due to the uncertainties in the luminosity measurement and in the cross-section estimate. The precision of the Standard Model prediction for the W^+W^- production cross-section estimate depends on the centre-of-mass energy and has been estimated to be of the order of 1%. An additional systematic error on the background rate arose from the preselection efficiency precision. The detailed study made in [22] could also be applied to this analysis, leading to a total uncertainty of 0.6%. The main contribution to this uncertainty is also the hadronisation model, with smaller contributions from the detector simulations. Combining these uncertainties the estimated precision of the four-fermion background rate at the preselection level was 1.3%.

Further systematic effects could have been introduced in the analysis when applying the relative mass difference cut and the likelihood background rejections. Any differences in the shapes of these variables between the real and simulated data would affect the efficiency of the cuts. Comparisons were made at early selection levels in order to keep the event rates high, enabling large statistics for the comparisons and keeping the signal-to-background rate so small that a possible signal in the data would not affect the distributions significantly. The uncertainty of the background rate due to the relative mass difference cut was estimated to be 1%. The effect of potential systematic effects of the shapes of the likelihood variable distributions was studied by changing the variable shapes in the simulation by reweighting simulated events. The reweighted events were propagated through the analysis and the effect on the cut efficiencies was studied. The uncertainty of the anti-$q\bar{q}$ likelihood and anti-WW cuts were estimated to be 2.3% and 0.7%. Uncertainties in the final discriminating likelihood shape, which would affect the signal likelihood of the data events, were also taken into account. A change in the

likelihood shape would influence the likelihood ratio in the exclusion limit calculation. This effect was taken into account by increasing the background rate uncertainty by an additional 2%.

Combination of all background uncertainties leads to a total uncertainty of 4% in the background normalisation. The uncertainty of the signal efficiency was estimated to be 2.5% with a 1% contribution from beam energy, hadronisation model etc., a 1.2% contribution from limited simulation statistics and a 2% contribution from the cuts and likelihoods.

In the $c\bar{s}\tau^-\bar{\nu}_\tau$ channel, the contribution to the systematic error from the uncertainties in the $q\bar{q}$ and W^+W^- total normalisation was estimated in a similar way to be 0.4% and 0.9%, respectively. The isolated lepton identification efficiency was estimated with the same di-lepton samples used for the $\tau^+\nu_\tau\tau^-\bar{\nu}_\tau$ channel, with a contribution of 1% both to the signal and background systematics. The uncertainties of the selection variables were estimated by comparing the shapes of the variable distributions in data and simulation at the preselection level. All variables agreed within statistical errors. Nevertheless, the potential error was estimated conservatively from the observed difference between real data and simulation when any particular cut was varied within the resolution of the corresponding variable. Combining these errors, a total uncertainty of 2.4% was estimated for the background rate and 0.3% in the signal efficiency. For the likelihood functions, the reweighting procedure described for $c\bar{s}c\bar{s}$ was followed, estimating the total contribution to 7.6% for the background and 3.2% for the signal.

For the $W^*A\tau^-\bar{\nu}_\tau$ and the W^*AW^*A channels, a similar procedure was followed, with an additional contribution from the b-tagging and with the difference that the W^+W^- is not the dominant background (described in detail in [32]). The total systematic errors on the signal efficiency for the W^*AW^*A and $W^*A\tau^-\bar{\nu}_\tau$ were 5% and 2% respectively. The relative errors on the background were 11% and 10%.

6   Results

The number of real data and background events and the estimated efficiencies in each of the analysis channels for different $H^\pm$ masses are summarised in Tables 7 and 8. The quoted errors include both statistic and systematic errors, added in quadrature.

6.1   Determination of the mass limit

No significant signal-like excess of events compared to the expected backgrounds was observed in any of the five final states investigated. Confidence levels were calculated using a modified frequentist technique, based on the extended maximum likelihood ratio [34, 35]. From these confidence levels, lower limits on the charged Higgs boson mass were derived at 95% confidence level in two scenarios. In the first scenario it was assumed that the charged Higgs boson decayed exclusively to either $\tau^-\bar{\nu}_\tau$ or $\bar{c}s$, corresponding to type II models. The limits were extracted as a function of the leptonic Higgs decay branching ratio $BR(H^- \to \tau^-\bar{\nu}_\tau)$. In the second scenario, corresponding to type I models, the W^*A decay was permitted if kinematically accessible and limits were computed for different values of M_A as a function of $\tan\beta$ or for different values of $\tan\beta$ as a function of M_A. The branching ratios were calculated according to [6] as functions of $\tan\beta$ and the neutral

pseudo-scalar and charged Higgs masses.

The background and signal probability density functions of one or two discriminating variables in each channel were used. The data samples collected at the different centre-of-mass energies were treated as independent channels. When there was a significant overlap between two channels, the one providing less sensitivity was ignored to avoid double counting. In the $c\bar{s}\bar{c}s$ and $c\bar{s}\tau^-\bar{\nu}_\tau$ channels the two discriminating variables were the reconstructed Higgs boson mass and the anti-WW likelihood. In the W^*AW^*A and $W^*A\tau^-\bar{\nu}_\tau$ the likelihood was replaced by the final neural network output. In the $\tau^+\nu_\tau\tau^-\bar{\nu}_\tau$ channel only the final background discrimination likelihood was used since mass reconstruction was not possible. The distributions of the discriminating variable for signal events, obtained from the simulation at different $H^\pm$ mass values for each $\sqrt{s}$, were interpolated for intermediate mass values.

The estimated uncertainties on background and signal were taken into account in the limit derivation by a Gaussian smearing around the central values of the number of expected events.

The resulting limits at 95% confidence level are shown in Figs. 13, 14 and 15 for the

Chan.	$\sqrt{s}$ (GeV)	lum.	data	total bkg.	ε_{75}	ε_{80}
$\tau^+\nu_\tau\tau^-\bar{\nu}_\tau$	189	153.8	14	17.8± 1.4	35.2±1.5%	35.7±1.5%
$\tau^+\nu_\tau\tau^-\bar{\nu}_\tau$	192	24.5	3	2.9± 0.2	33.6±1.5%	37.0±1.5%
$\tau^+\nu_\tau\tau^-\bar{\nu}_\tau$	196	72.4	10	9.1± 0.7	33.6±1.5%	37.0±1.5%
$\tau^+\nu_\tau\tau^-\bar{\nu}_\tau$	200	81.8	10	9.7± 0.8	32.3±1.5%	35.5±1.5%
$\tau^+\nu_\tau\tau^-\bar{\nu}_\tau$	202	39.4	2	4.7± 0.4	32.3±1.5%	35.5±1.5%
$\tau^+\nu_\tau\tau^-\bar{\nu}_\tau$	205	69.1	10	8.5± 0.6	32.2±1.5%	33.4±1.5%
$\tau^+\nu_\tau\tau^-\bar{\nu}_\tau$	206.6	79.8	5	10.1± 0.8	32.2±1.5%	33.4±1.5%
$\tau^+\nu_\tau\tau^-\bar{\nu}_\tau$	206.3(S6)	50.0	5	6.1± 0.5	31.7±1.5%	35.7±1.5%
$c\bar{s}\bar{c}s$	189	158.0	565	554.9±22.2	52.1±1.3%	52.6±1.3%
$c\bar{s}\bar{c}s$	192	25.9	90	93.1± 3.7	54.6±1.4%	54.1±1.4%
$c\bar{s}\bar{c}s$	196	76.9	284	279.7±11.2	54.6±1.4%	54.1±1.4%
$c\bar{s}\bar{c}s$	200	84.3	299	300.6±12.2	53.1±1.3%	53.9±1.3%
$c\bar{s}\bar{c}s$	202	41.1	147	136.5± 5.5	53.1±1.3%	53.9±1.3%
$c\bar{s}\bar{c}s$	205	75.6	270	264.5±10.6	51.5±1.3%	53.6±1.3%
$c\bar{s}\bar{c}s$	206.6	87.8	291	288.3±11.5	52.1±1.3%	53.5±1.3%
$c\bar{s}\bar{c}s$	206.3 (S6)	60.8	168	196.9± 7.9	51.5±1.3%	53.6±1.3%
$c\bar{s}\tau^-\bar{\nu}_\tau$	189	153.8	296	285.8±22.9	57.5±2.7%	57.1±2.7%
$c\bar{s}\tau^-\bar{\nu}_\tau$	192	24.5	56	47.5± 3.8	57.6±2.7%	56.5±2.7%
$c\bar{s}\tau^-\bar{\nu}_\tau$	196	72.4	147	143.8±11.5	57.6±2.7%	56.5±2.7%
$c\bar{s}\tau^-\bar{\nu}_\tau$	200	81.8	158	154.6±12.4	57.4±2.7%	57.3±2.7%
$c\bar{s}\tau^-\bar{\nu}_\tau$	202	39.4	71	75.7± 6.1	57.4±2.7%	57.3±2.7%
$c\bar{s}\tau^-\bar{\nu}_\tau$	205	69.1	130	129.5±10.4	57.2±2.7%	55.5±2.6%
$c\bar{s}\tau^-\bar{\nu}_\tau$	206.6	79.8	139	150.4±12.0	57.2±2.7%	55.5±2.6%
$c\bar{s}\tau^-\bar{\nu}_\tau$	206.3(S6)	50.0	88	94.4± 7.6	57.7±2.7%	55.9±2.6%

Table 7: Integrated luminosity, observed number of events, expected number of background events and signal efficiency (for 75 GeV/c^2 and 80 GeV/c^2 charged Higgs boson masses) for different centre-of-mass energies for the channels not involving W^*A decays.

Chan.	$\sqrt{s}$ (GeV)	lum.	data	total bkg.	ε_{80}	ε_{90}
$W^*A\tau^-\bar{\nu}_\tau$	189	153.8	12	11.4± 0.7	20.5±2.2%	10.2±2.1%
$W^*A\tau^-\bar{\nu}_\tau$	192	24.5	3	1.6± 0.1	20.1±2.2%	11.4±2.1%
$W^*A\tau^-\bar{\nu}_\tau$	196	72.4	2	4.7± 0.3	20.1±2.2%	11.4±2.1%
$W^*A\tau^-\bar{\nu}_\tau$	200	81.8	4	4.9± 0.3	21.0±2.2%	13.7±2.1%
$W^*A\tau^-\bar{\nu}_\tau$	202	39.4	4	2.5± 0.2	21.0±2.2%	13.7±2.1%
$W^*A\tau^-\bar{\nu}_\tau$	205	69.1	4	4.1± 0.2	21.3±2.2%	15.5±2.2%
$W^*A\tau^-\bar{\nu}_\tau$	206.6	79.8	6	4.6± 0.3	21.3±2.2%	15.5±2.2%
$W^*A\tau^-\bar{\nu}_\tau$	206.3(S6)	50.0	4	3.0± 0.2	21.3±2.2%	15.5±2.2%
W^*AW^*A	189	158.0	81	79.7± 7.9	35.6±5.1%	39.4±5.1%
W^*AW^*A	192	25.9	16	13.0± 1.3	35.6±5.1%	39.4±5.1%
W^*AW^*A	196	76.9	37	35.3± 3.5	35.6±5.1%	39.4±5.1%
W^*AW^*A	200	84.3	36	35.6± 3.6	35.5±5.1%	39.3±5.1%
W^*AW^*A	202	41.1	16	17.7± 1.8	35.5±5.1%	39.3±5.1%
W^*AW^*A	205	75.6	24	24.7± 2.5	37.8±5.1%	34.5±5.1%
W^*AW^*A	206.6	87.8	30	28.3± 2.8	37.8±5.1%	34.5±5.1%
W^*AW^*A	206.3(S6)	60.8	13	18.2± 2.8	37.8±5.1%	34.5±5.1%

Table 8: Integrated luminosity, observed number of events, expected number of background events and signal efficiency (80 GeV/c^2 and 90 GeV/c^2 charged Higgs boson masses, and M_A=12 GeV/c^2) for different centre-of-mass energies for the channels involving W^*A decays.

two scenarios as functions of the model parameters. The expected lower limits on the mass have been obtained as the median[7] of a large number of simulated experiments.

If the W^*A decay is forbidden, a lower $H^\pm$ mass limit of $M_H > 74.4$ GeV/c^2 can be set at 95% confidence level, for any branching ratio BR(H $\to \tau^-\bar{\nu}_\tau$). The lower mass limit corresponds to a branching ratio of about 0.3. The minimum of the expected limits is 76.3 GeV/c^2. The noticeable difference between observed and expected limits is dominated by a small unexcluded region (Fig. 13) around BR=0.35 produced by a small excess of data in that region in the semileptonic channel. However, this region is excluded at 92% confidence level,

Within type I models, a lower limit on the $H^\pm$ mass of $M_H > 76.7$ GeV/c^2 can be set at 95% confidence level, for any $\tan\beta$ for $M_A > 12$ GeV/c^2. The expected lower limit on the mass for these conditions was 77.1 GeV/c^2. Table 9 shows the limits obtained for different values of M_A and $\tan\beta$. The lower limit on the mass for a given M_A or a given $\tan\beta$ and the absolute lower limit are also shown.

Figures 16 and 17 show the observed and expected confidence level for the background only hypothesis[8]. In general a good agreement with this hypothesis is found, with the confidence levels inside the two standard deviation regions. This is true in all cases, except in a small mass region below 45 GeV/c^2 for the $c\bar{s}\bar{c}s$ decay channel, where the

---

[7] The median is calculated as the value which has 50% of the limits of the simulated experiments below it and similarly, the $\pm 1\sigma$ estimations correspond to 84% and 16% of the simulated experiments.

[8] The confidence level for background hypothesis, CL_b is defined [34, 35] in such a way that its expectation value is 0.5 in the absence of signal. A CL_b value close to 1 indicates a signal-like excess of candidates in the data.

M_A	$\tan\beta = 0.01$	$\tan\beta = 50$	minimum
12	82.4 (80.7)	82.1 (83.5)	77.6 (77.1)
30	82.5 (80.7)	84.6 (86.3)	78.6 (77.6)
50	82.5 (80.7)	88.0 (89.2)	78.9 (78.4)
70	82.5 (80.6)	86.4 (88.0)	80.2 (79.0)
minimum	82.4 (80.6)	79.8 (79.9)	76.7 (77.1)

Table 9: Observed limits for the charged Higgs mass in GeV/c^2 at 95% C.L. for different values of M_A (in GeV) and $\tan\beta$. The expected median limit is shown in parenthesis. The last column and the last row, show the worst case limits for a fixed mass and any $\tan\beta$ or a fixed $\tan\beta$ and any mass.

observed confidence level corresponds to 3.1 standard deviations. This excess, however, was not found to be compatible with a charged Higgs signal and therefore considered as a fluctuation for the following reasons. Firstly, the excess is an order of magnitude smaller than the expected rate from a signal. Secondly, the excess is distributed over much broader mass range than what would be expected for a charged Higgs signal. As a consequence, the signal plus background hypothesis is incompatible with the data with a confidence level equivalent to more than 13 standard deviations.

6.2 Cross-section limit

The results are also expressed as 95% confidence level upper limits for the charged Higgs boson production cross-section as a function of the charged Higgs boson mass, for different assumptions on the model parameters, i.e. leptonic branching ratio for the first scenario and M_A and $\tan\beta$ for the second. These cross-section limits were determined for each mass point by scaling the expected Two Higgs Doublet Model signal cross-section up or down until the confidence level for signal hypothesis reached 95%. Therefore the only assumption taken from the model is the dependence of the cross-section on the mass and centre-of-mass energy and thus this approach can be considered model independent to a large extent. Results are summarised in Figures. 18 and 19. These cross-sections are given for 206.6 GeV centre-of-mass energy, the maximum energy for which this analysis has a sizable luminosity.

7 Conclusions

A search for pair-produced charged Higgs bosons was performed using the data collected by DELPHI at LEP at centre-of-mass energies from 189 GeV to 209 GeV searching for the $\tau^+\nu_\tau\tau^-\bar{\nu}_\tau$, $c\bar{s}\bar{c}s$, $c\bar{s}\tau^-\bar{\nu}_\tau$, W*AW*A and W*A$\tau^-\bar{\nu}_\tau$ final states. No significant excess of candidates over the expected Standard Model background was observed and lower limits on the charged Higgs boson mass were set in two scenarios. Assuming that the branching ratio to W*A is negligible (type II models or type I with a heavy neutral pseudo-scalar) limits are set at 95% confidence level as a function of the branching ratio to leptons. Results are shown in Fig. 13. The absolute limit is 74.4 GeV/c^2 at 95% confidence level. Limits were also set within type I models for different neutral pseudo-scalar masses,

$M_A > 12$ GeV/c^2 and $\tan\beta$. Results are shown in Figures 14 and 15. The absolute limit is 76.7 GeV/c^2 at 95% confidence level.

To allow a less model dependent comparison limits are also expressed in terms of upper bounds on the cross-section for different sets of the model parameters. Results are shown in Figs. 18 and 19.

This analysis improves previous searches both by the inclusion of new discriminant techniques and by the less model dependent approach allowing more sensitivity and covering a wider range of models and model parameters.

Acknowledgments

References

[1] J. Abdallah *et al.* (DELPHI Collaboration), Phys. Lett. **B 525** (2002) 17;
P. Abreu *et al.* (DELPHI Collaboration), Phys. Lett. **B 460** (1999) 484.

[2] R. Barate *et al.* (ALEPH Collaboration), Phys. Lett. **B 487** (2000) 253;
M. Acciarri *et al.* (L3 Collaboration), Phys. Lett. **B 496** (2000) 34;
G. Abbiendi *et al.* (OPAL Collaboration), Eur. Phys. J. **C 7** (1999) 407.

[3] H.E. Haber *et al.*, Nucl. Phys. **B 161** (1979) 493.

[4] S.L. Glashow and S. Weinberg, Phys. Rev. **D15** (1977) 1958;
E.A. Paschos, Phys. Rev. **D15** (1977) 1966.

[5] J. Abdallah *et al.* (DELPHI Collaboration), "Searches for Neutral Higgs Bosons in Extended Models", to be submitted to Eur. Phys. J.

[6] A.G. Akeroyd Nucl. Phys. **B 544** (1999) 557;
A.G. Akeroyd *et al.*, Eur. Phys. J. **C 20** (2001) 51.

[7] P. Abreu *et al.* (DELPHI Collaboration), Zeit. Phys. **C64** (1994) 183.

[8] The LEP Collaboration *et al.*, "A combination of preliminary electroweak measurements...", **CERN−EP−2002−091** (2002)[hep-ex/0212036].

[9] P.J. Franzini and P. Taxil, Higgs search (Z physics at LEP vol 2), **CERN−89−08** (1989)

[10] P. Aarnio *et al.* (DELPHI Collaboration), Nucl. Instr. and Meth. **A 303** (1991) 233.

[11] P. Abreu *et al.* (DELPHI Collaboration), Nucl. Instr. and Meth. **A 378** (1996) 57.

[12] S. Jadach, B.F.L. Ward, Z. Was, Comp. Phys. Comm. **130** (2000) 260.

[13] S. Jadach, B.F.L. Ward, Z. Was, Comp. Phys. Comm. **79** (1994) 503.

[14] S. Jadach, W. Placzek and B.F.L. Ward, Phys. Lett. **B390** (1997) 298.

[15] E. Accomando and A. Ballestrero, Comp. Phys. Comm. **99** (1997) 270;
E. Accomando, A. Ballestrero and E. Maina, [hep-ph/0204052], accepted by Comp. Phys. Commun.

[16] S. Nova, A. Olchevski and T. Todorov, **CERN-96-01** , Vol. 2. p. 224;
T. Alderweireld *et al.*, **CERN-2000-009**, p. 219.

[17] F.A. Berends, P.H. Daverveldt, R. Kleiss, Comp. Phys. Comm. **40** (1986) 271, 285 and 309.

[18] T. Sjöstrand, Comp. Phys. Comm. **82** (1994) 74.

[19] G. Marchesini *et al.*, Comp. Phys. Comm. **67** (1992) 465.

[20] L. Lönnblad, Comp.Phys.Comm. **71** (1992) 15.

[21] P. Janot, **CERN-96-01** , Vol. 2, p. 309.

[22] P. Abreu *et al.* (DELPHI Collaboration), Phys. Lett. **B 479** (2000) 89;
J. Abdallah *et al.* (DELPHI Collaboration), "Measurement of the W-pair Production
Cross-section and W Branching Ratios in e⁻e⁺ collisions at $\sqrt{s} = $ 161-209 GeV", to
be submitted to Eur. Phys. J. C.

[23] M. Davier *et al.*, Phys. Lett. **B306** (1993) 411;
A. Rougé, Zeit. Phys. **C48** (1990) 75.

[24] P. Abreu *et al.* (DELPHI Collaboration), Zeit. Phys. **C 67** (1995) 183.

[25] S. Catani *et al.*, Phys. Lett. **B 269** (1991) 432.

[26] P. Abreu *et al.* (DELPHI Collaboration), Phys. Lett. **B 439** (1998) 209.

[27] M. Battaglia and P. M. Kluit, Nucl. Instr. and Meth. **A 433** (1999) 252.

[28] P.Abreu *et al.* (DELPHI Collaboration), Eur. Phys. J. **C 2** (1998) 581.

[29] P. Abreu **CERN-96-01** , Nucl. Instr. & Meth. **A427** (1999) 487.

[30] P. Abreu *et al.* (DELPHI Collaboration), Phys. Lett. **B 502** (2001) 9.

[31] J. Abdallah *et al.* (DELPHI Collaboration), **CERN EP** 2002-088 (2 October 2002),
submitted to Eur. Phys. J. C.

[32] J. Abdallah *et al.* (DELPHI Collaboration), Eur. Phys. J. **C 22** (2001) 17.

[33] P.Abreu *et al.* (DELPHI Collaboration), Eur. Phys. J. **C10** (1999) 563.

[34] A.L. Read, **CERN-2000-005**, p. 81

[35] J. Abdallah *et al.* (DELPHI Collaboration), "Final results from DELPHI on the
searches for SM and MSSM Neutral Higgs Boson", **CERN EP** 2003-008 (11 February
2003), submitted to Eur. Phys. J. C.

DELPHI
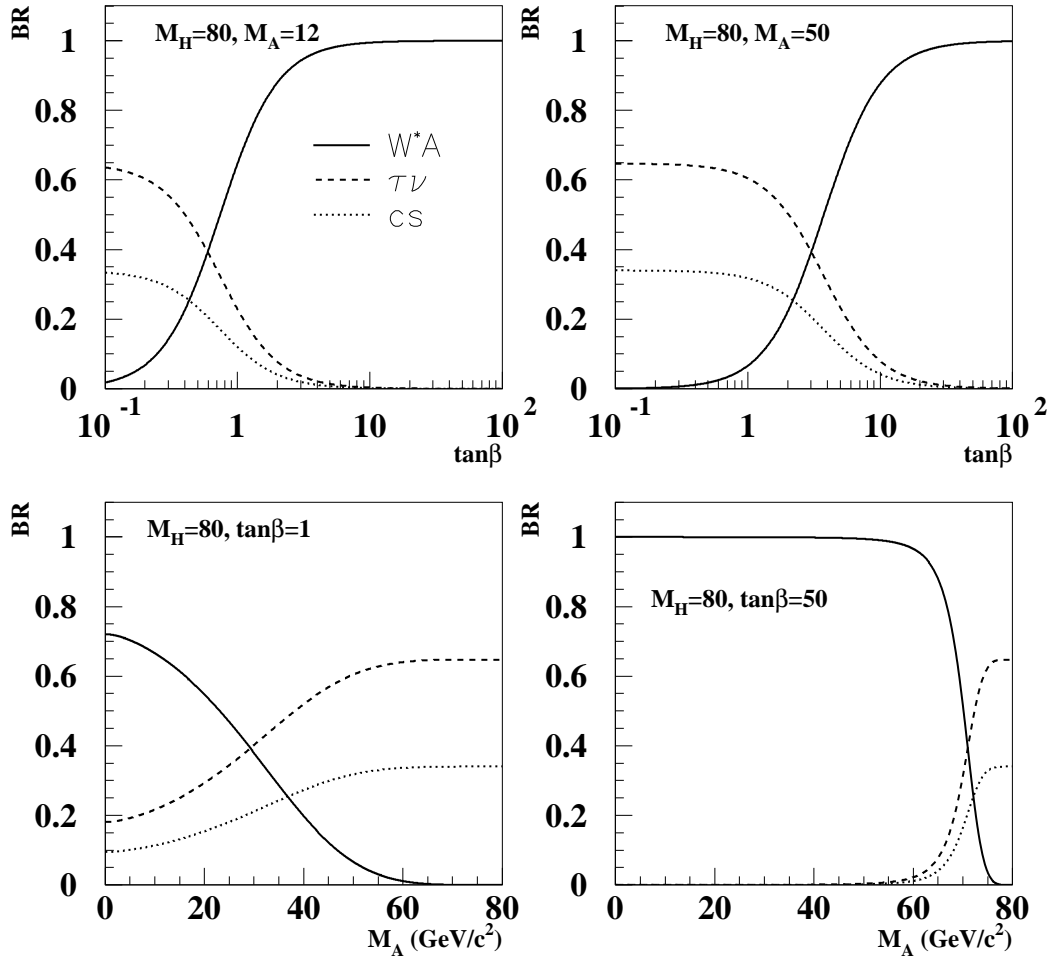
Figure 1: Predicted charged Higgs boson decay branching ratios for different parameters in the framework of type I Two Higgs Doublets Models.
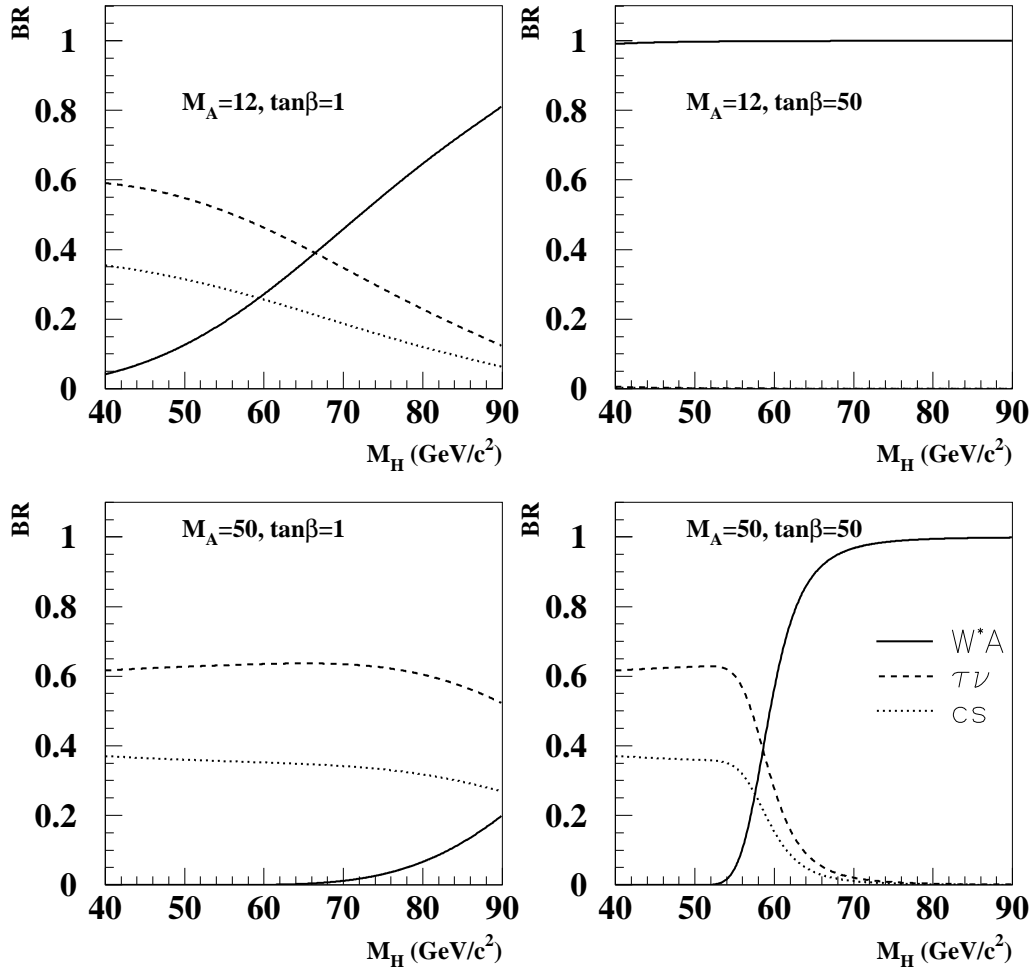
DELPHI

Figure 2: Predicted charged Higgs boson decay branching ratios for different parameters in the framework of type I Two Higgs Doublets Models.

DELPHI
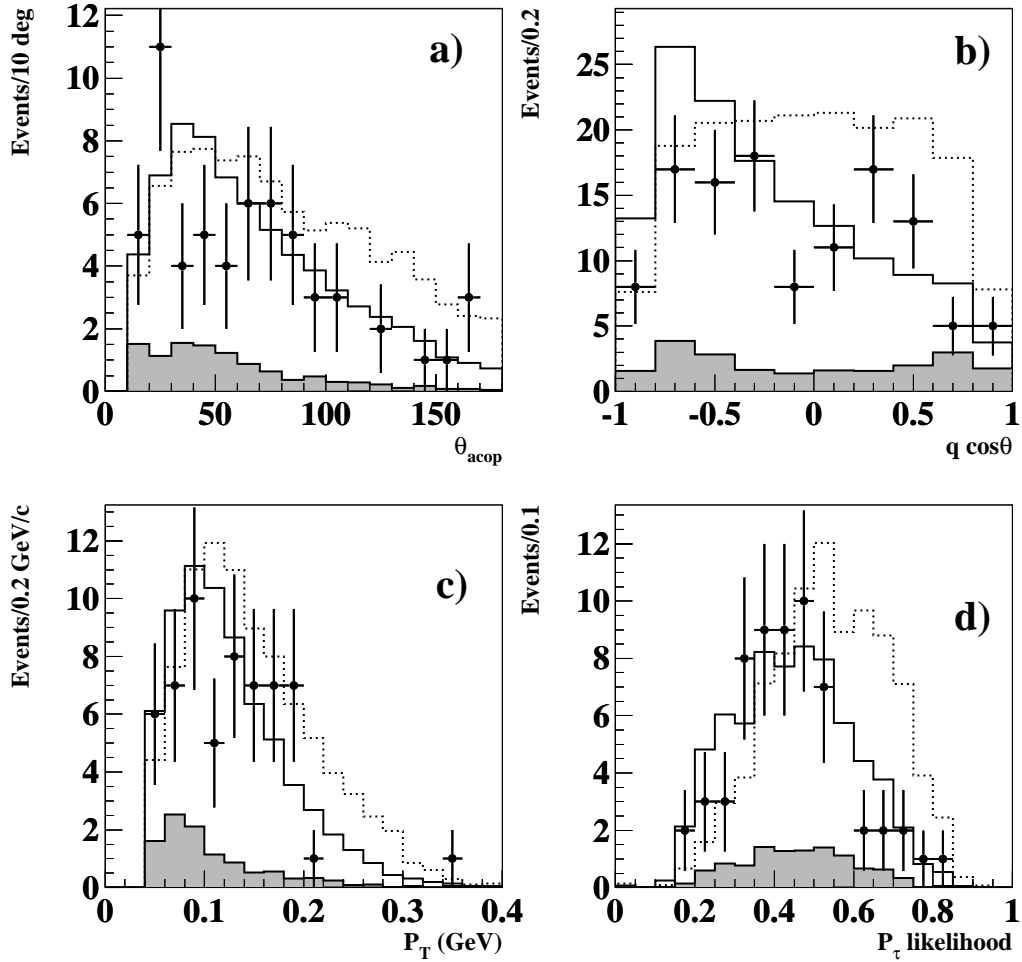
Figure 3: Distribution of some of the variables used for the anti-WW likelihood for the $\tau^+\nu_\tau\tau^-\bar{\nu}_\tau$ analysis at $\sqrt{s} = 189$–209 GeV after preselection: a) acoplanarity, b) signed cosine of polar angle of each τ candidate, c) total transverse momentum and d) event τ polarisation likelihood. Data are shown as filled circles, while the solid histogram contour shows the expected SM background with contributions from W^+W^- (unfilled) and $q\bar{q}$ (shaded). The expected histogram for a 85 GeV/c^2 charged Higgs boson signal is shown as a dashed line with arbitrary normalisation for comparison.
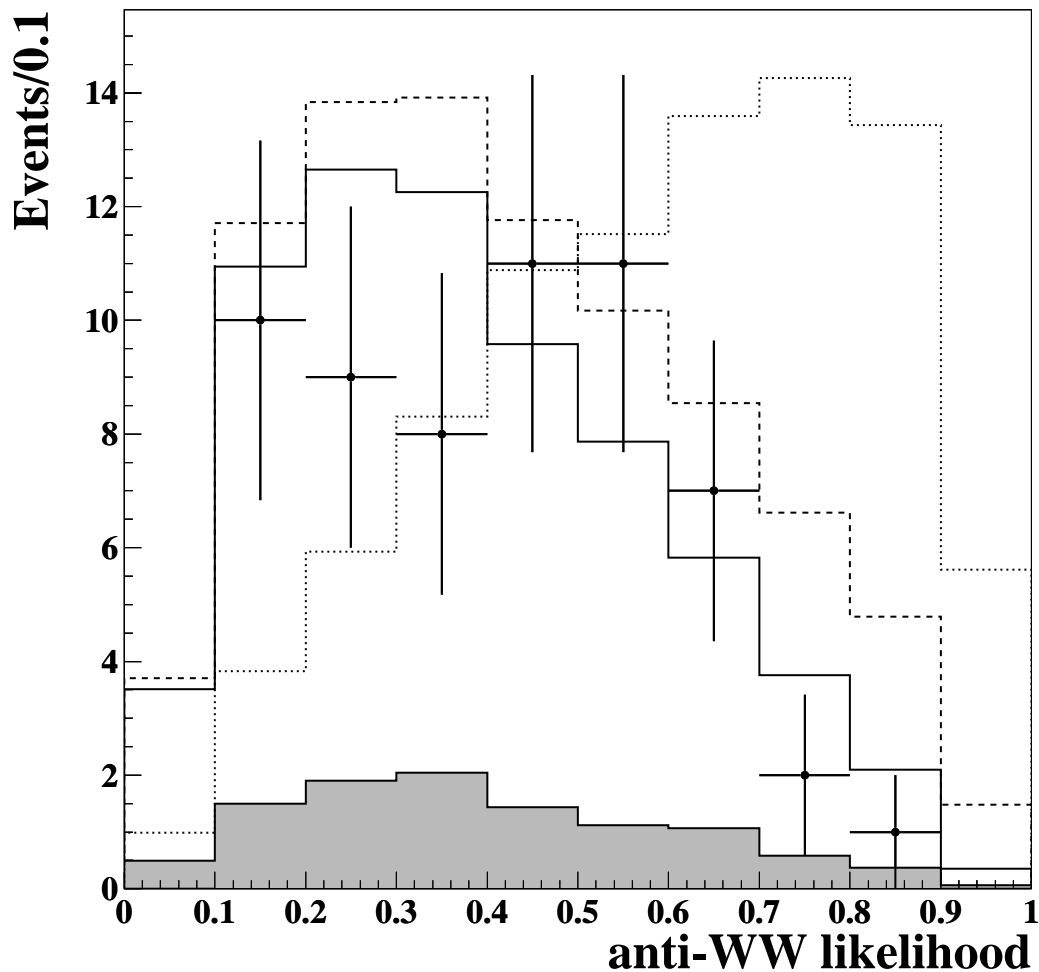
Figure 4: Distribution of the anti-WW likelihood for the $\tau^+\nu_\tau\tau^-\bar{\nu}_\tau$ analysis at 189–209 GeV. The dots represent the data, while the solid histogram contour shows the expectation from SM processes, as in Fig. 3. The expected histogram for a 85 GeV/c^2 charged Higgs boson signal has been normalised to the production cross-section and 100% leptonic branching ratio and added to the backgrounds (dashed). The dotted line shows the shape of the likelihood for the charged Higgs signal only in arbitrary normalization.
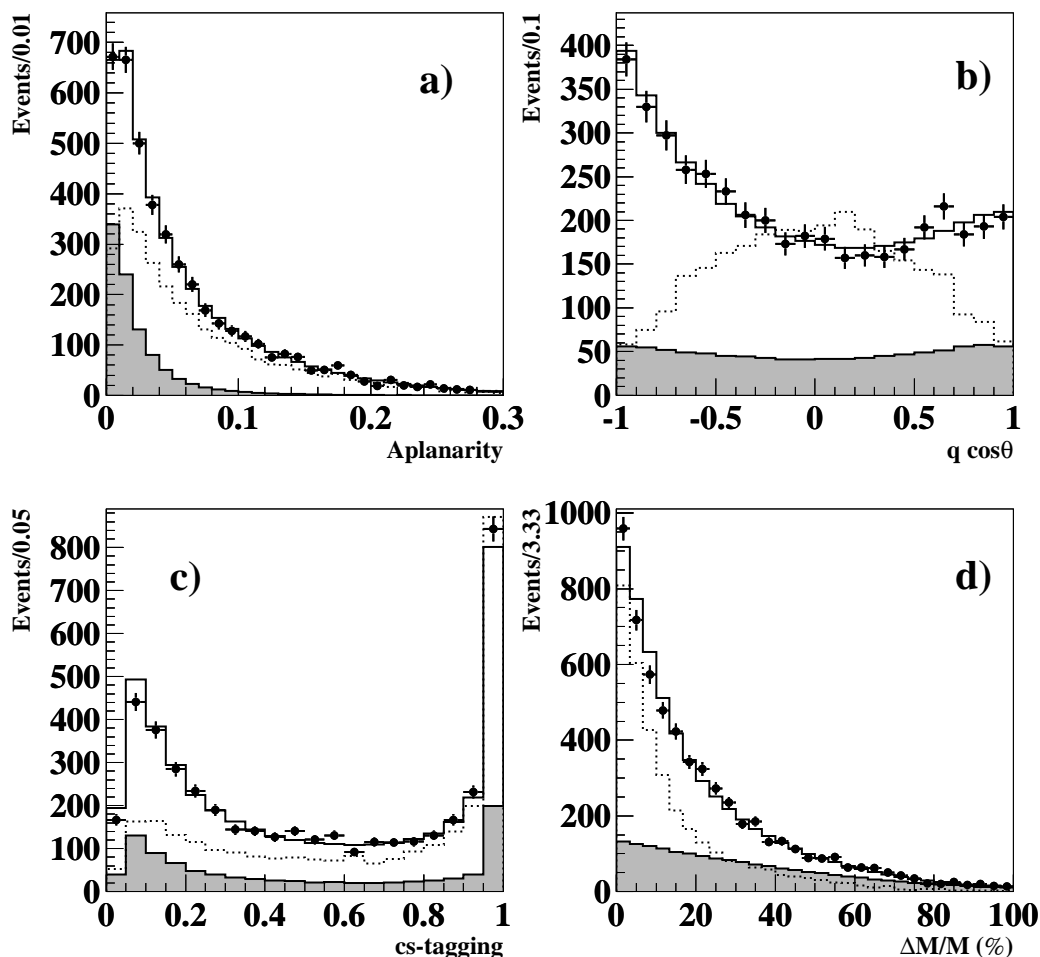
Figure 5: Distribution of some of the variables used for the anti-q$\bar{q}$ and anti-WW likelihoods in the c$\bar{s}\bar{c}$s analysis at $\sqrt{s}$ =189–209 GeV after preselection: a) aplanarity, b) signed cosine of the polar angle of the boson c) $\bar{c}$s-tagging variable and d) mass difference. Data are shown as filled circles, while the solid histogram shows the expected SM background with contributions from W$^+$W$^-$ (unfilled) and q$\bar{q}$ (shaded). The expected distribution for a 75 GeV/c^2 charged Higgs boson signal is shown as a dotted histogram with arbitrary normalisation for comparison.
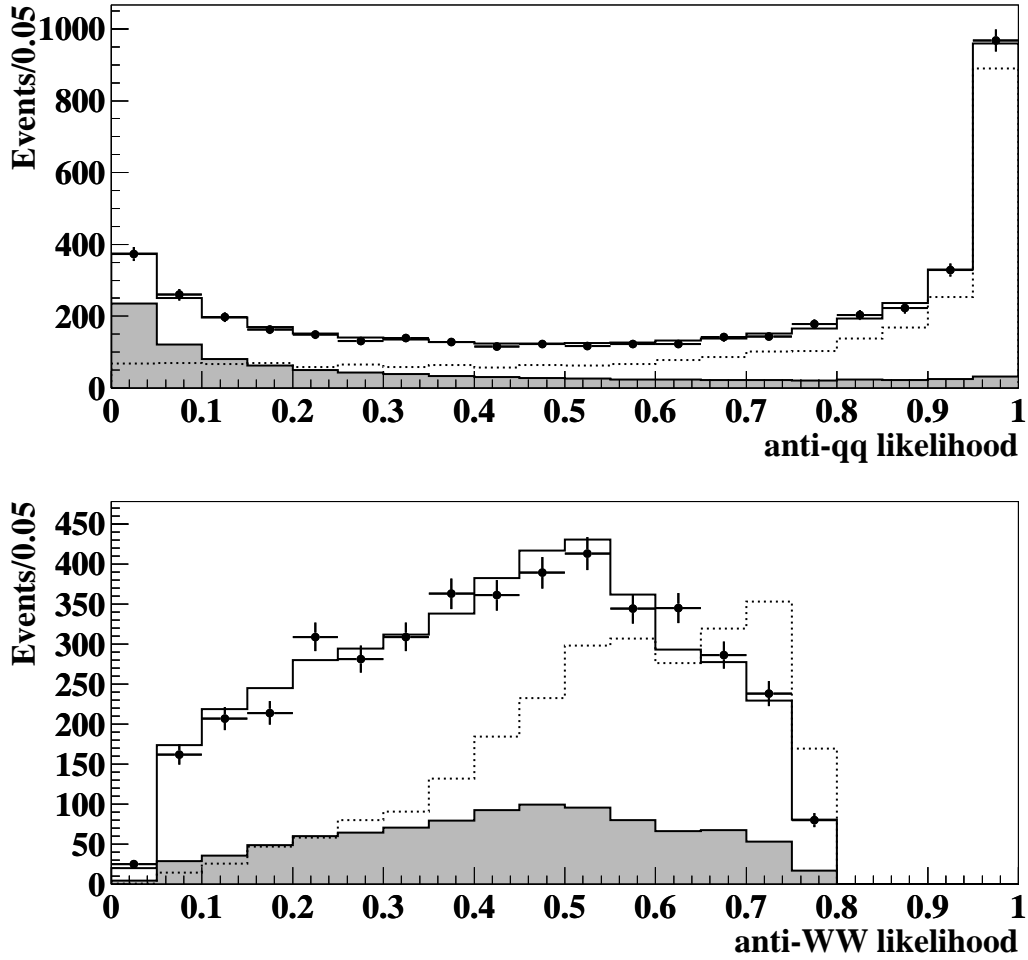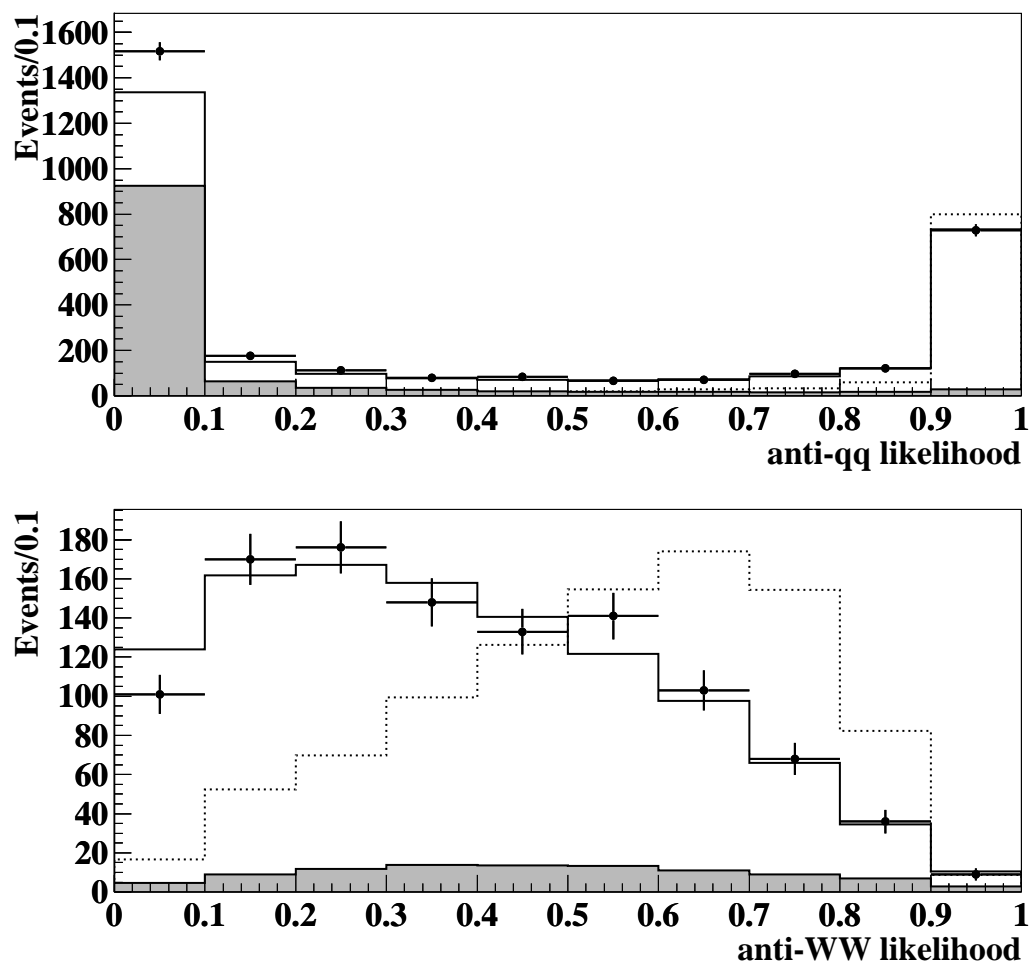
Figure 6: Distributions of the anti-q$\bar{q}$ (top) and anti-WW (bottom) likelihoods in the c$\bar{s}$c$\bar{s}$ analysis at 189–209 GeV after preselection and mass difference cut. Data and expected SM backgrounds are indicated as in Fig. 5. The expected distribution for a 75 GeV/c^2 charged Higgs boson signal is shown as a dotted histogram with arbitrary normalisation.
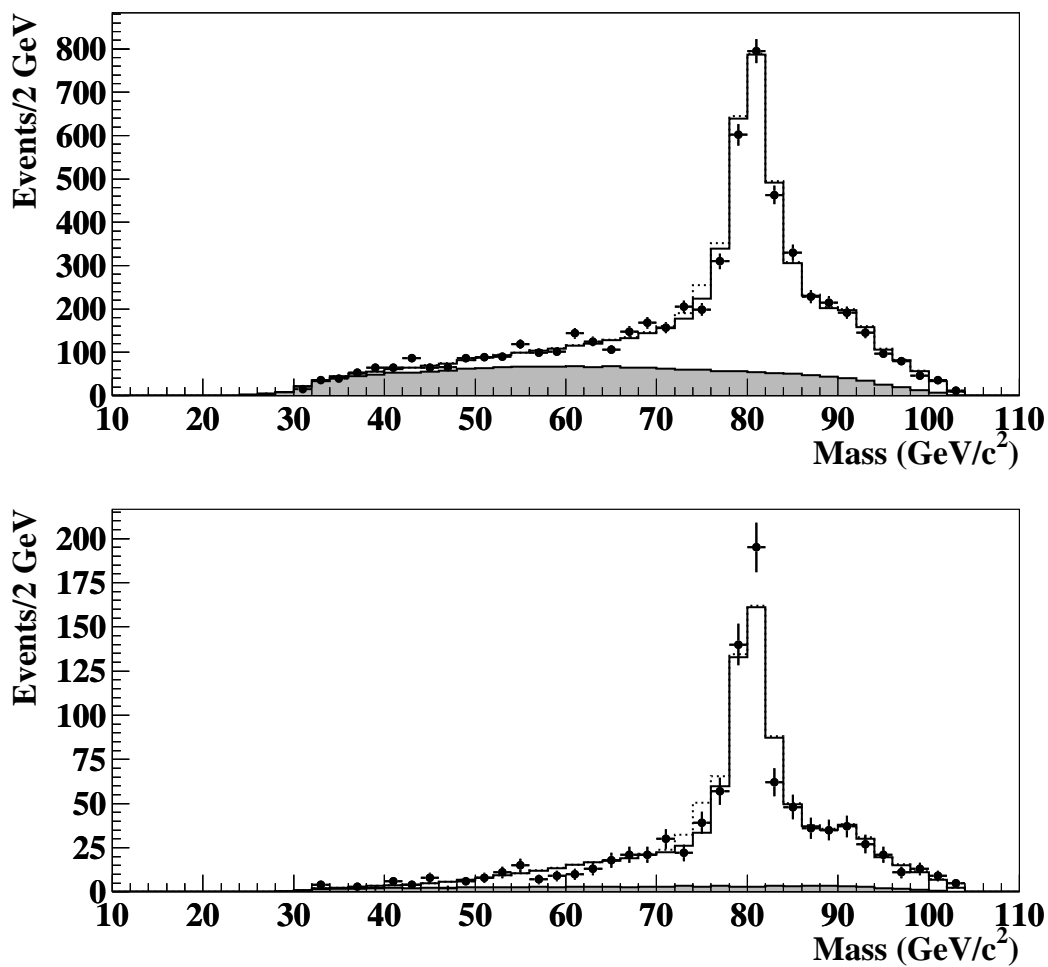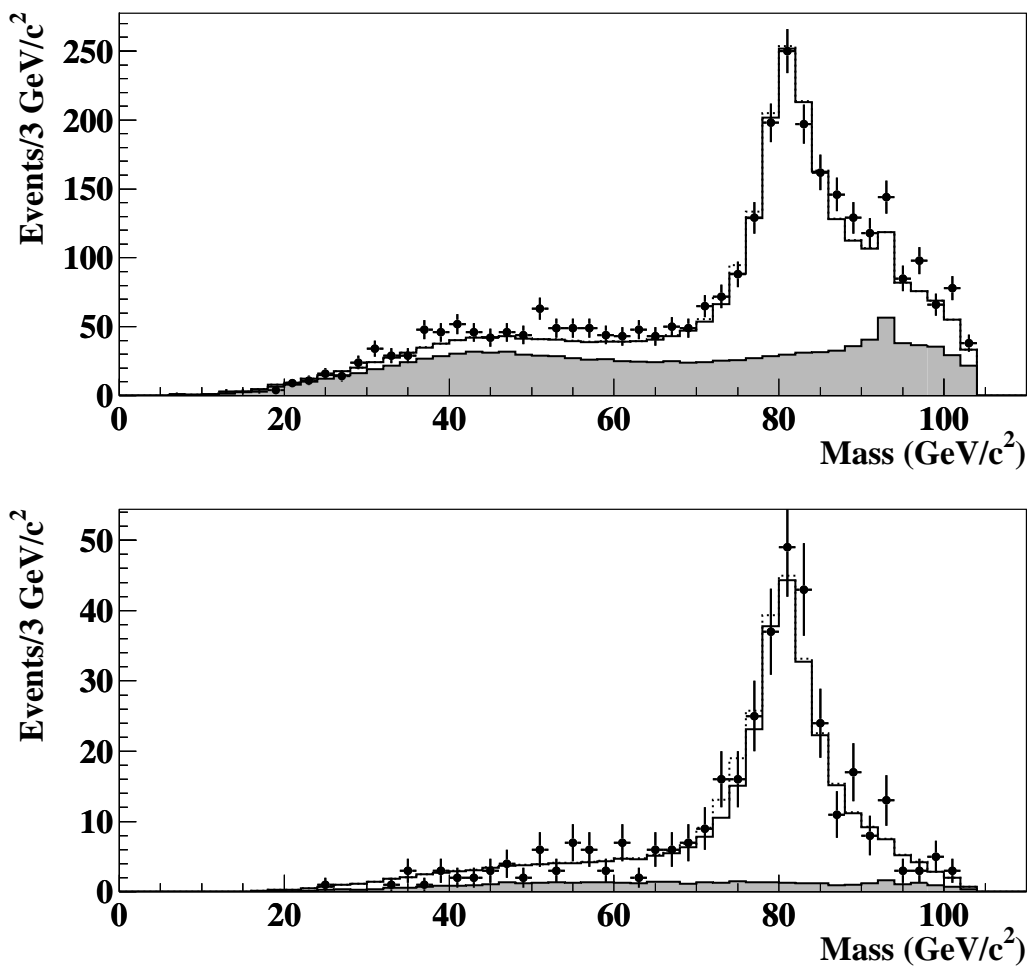
Figure 7: Reconstructed mass distribution in the c$\bar{\text{s}}$$\bar{\text{c}}$s analysis at $\sqrt{s}$ = 189–209 GeV at preselection (top) and at the final selection with additional cut of $\mathcal{L}_{\text{qq}}$ > 0.7 and $\mathcal{L}_{\text{WW}}$ > 0.5 (bottom). Data are shown as filled circles, while the solid histogram shows the expected SM background with contributions from W$^+$W$^-$ (unfilled) and q$\bar{\text{q}}$ (shaded). The expected distribution in the presence of an H$^+$H$^-$ signal, with M$_{\text{H}}$ = 75 GeV/c^2 and hadronic branching ratio of 100%, is also shown for comparison (dotted).
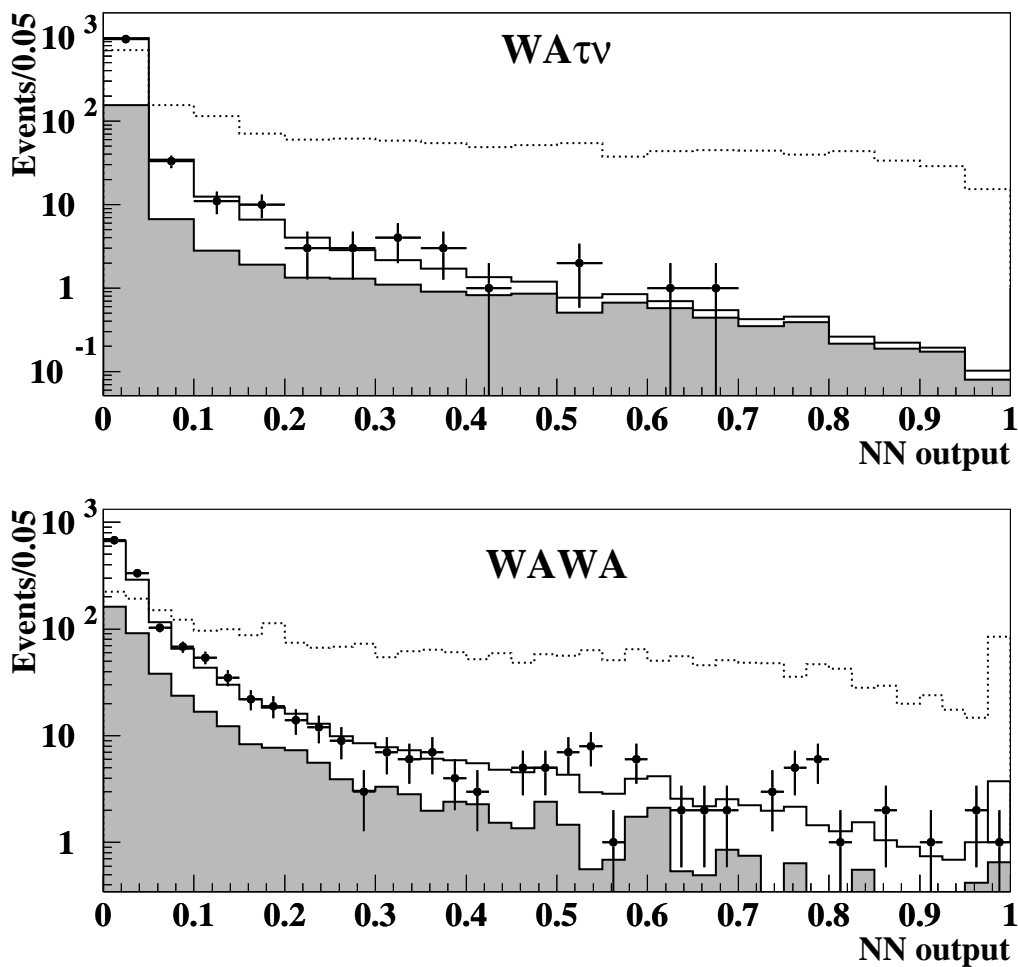
DELPHI
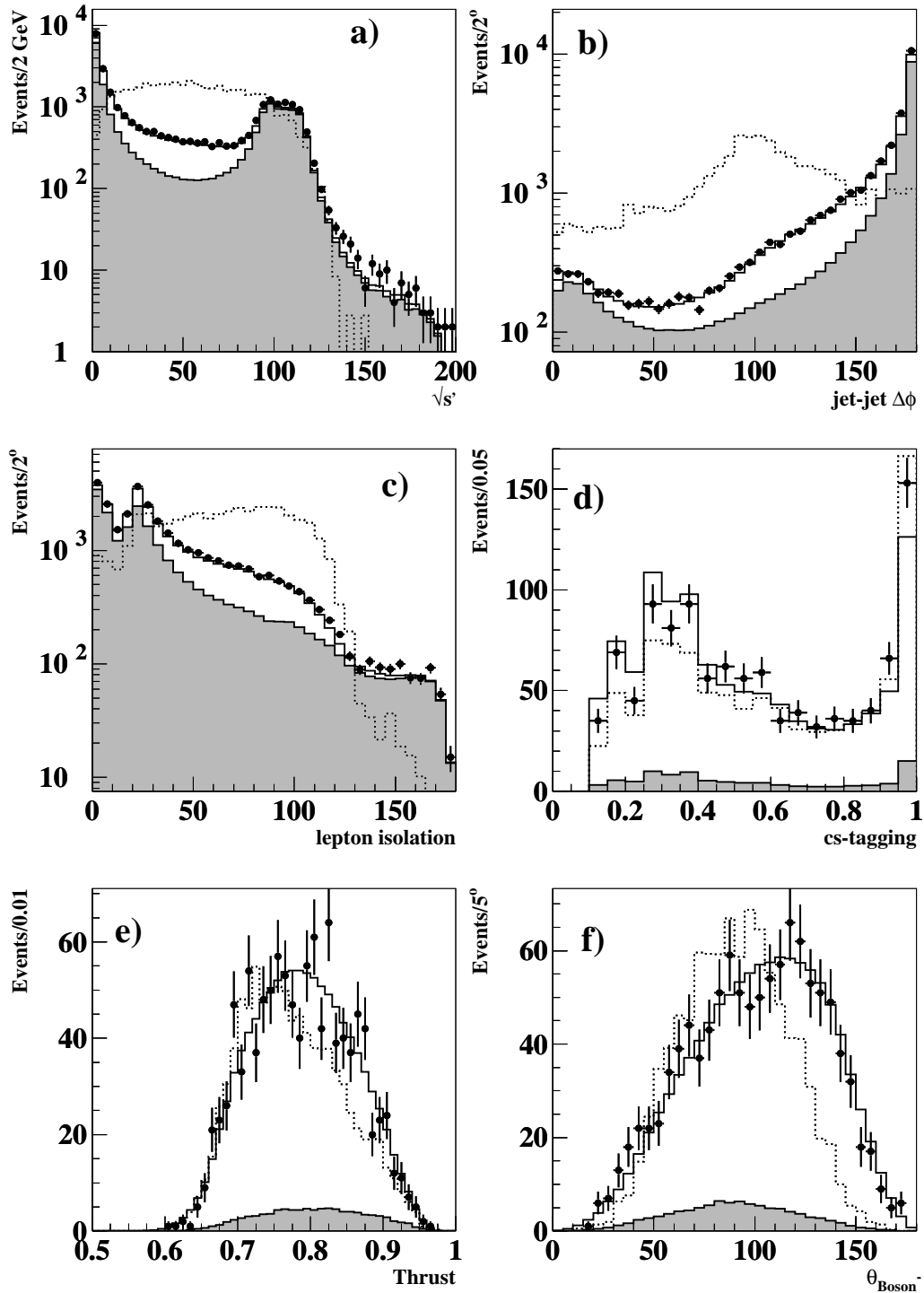
Figure 8: Distributions at preselection level of some of the variables used in the $c\bar{s}\tau^-\bar{\nu}_\tau$ analysis. The effective centre-of-mass energy (a), acoplanarity of hadronic jets (b), and the lepton isolation (c) used in the anti-q$\bar{q}$ likelihood. The $\bar{c}$s-tagging variable (d), the thrust (e), and the angle of the negatively charged boson (f) used in the anti-WW likelihood. Data are shown as filled circles, while the solid histogram contour shows the expected SM background with contributions from W^+W^- (unfilled) and q$\bar{q}$ (shaded). The expected histogram for a 75 GeV/c^2 charged Higgs boson signal is shown as a dotted histogram with arbitrary normalisation for comparison.

Figure 9: Distributions of the anti-q$\bar{\text{q}}$ and anti-WW likelihoods for the c$\bar{\text{s}}\tau^-\bar{\nu}_\tau$ analysis at 189–209 GeV. The anti-q$\bar{\text{q}}$ likelihood is plotted after preselection and the anti-WW likelihood at the final level. Data and SM background are indicated as in Fig. 8. The expected distribution for a 75 GeV/c^2 charged Higgs boson signal is shown as a dotted histogram with arbitrary normalisation.

Figure 10: Reconstructed mass distribution for events selected in the $c\bar{s}\tau^-\bar{\nu}_\tau$ analysis at 189–209 GeV at preselection (top) and at the final selection level (bottom), with an additional cut on the anti-WW likelihood $\mathcal{L}_{WW} > 0.5$. Data and SM background are indicated as in Fig. 8. The expected distribution in the presence of an H^+H^- signal, with $M_H = 75$ GeV/c^2 and leptonic branching ratio of 50%, is also shown for comparison (dotted).

Figure 11: Distribution of the output of the final discriminating neural network for events selected in the W*A$\tau^-\bar{\nu}_\tau$ (top) and W*AW*A (bottom) analyses, respectively, for energies between 189–209 GeV. The data and the simulated SM background are indicated as in previous figures. The expected distribution in the presence of an H$^+$H$^-$ signal, with M$_H$ = 80 GeV/c^2 and M$_A$ = 30 GeV/c^2, is also shown in arbitrary normalisation for comparison (dotted).
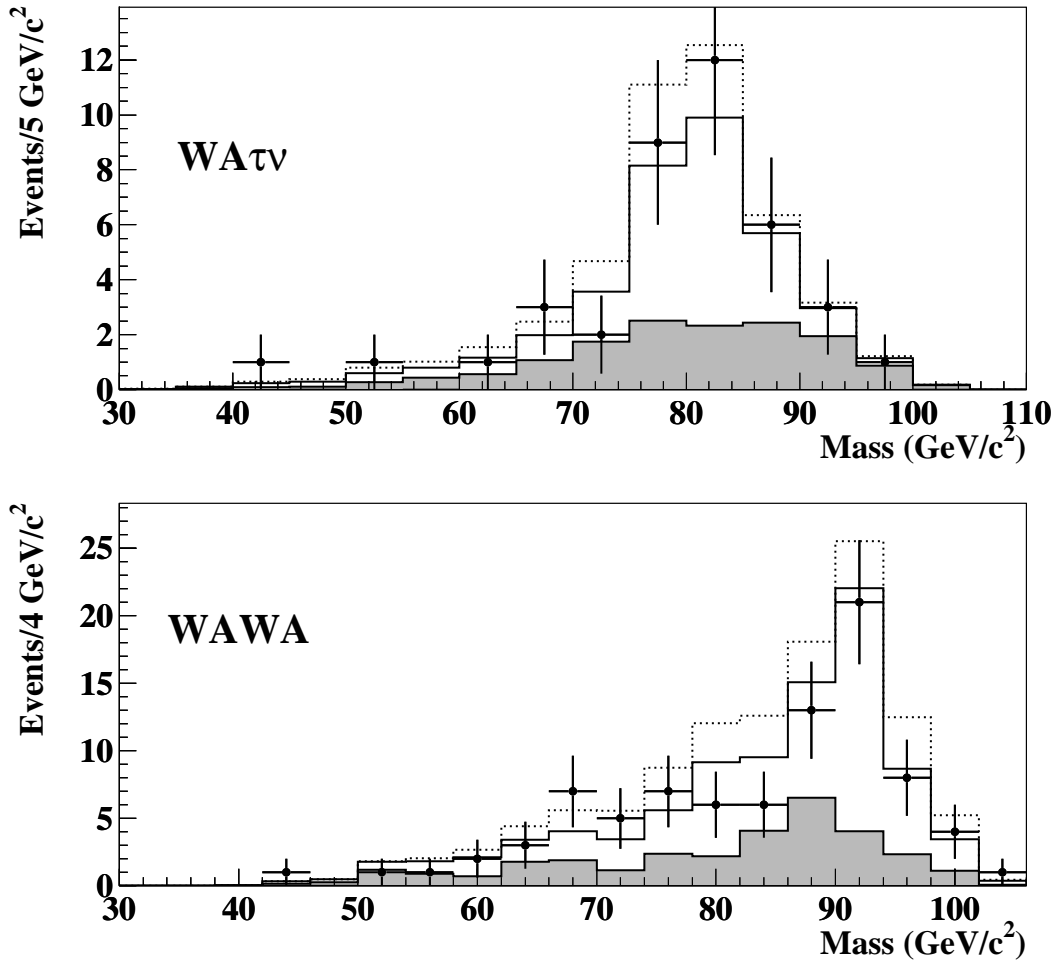
Figure 12: Reconstructed mass distribution for events selected in the $W^*A\tau^-\bar{\nu}_\tau$ (top) and W^*AW^*A (bottom) analyses by a cut on the neural network output of 0.1 and 0.3, respectively, for energies between 189–209 GeV. The data and the simulated SM background are indicated as in previous figures. The expected distribution in the presence of an H^+H^- signal, with $M_H = 80$ GeV/c^2 and $M_A = 30$ GeV/c^2, is also shown for comparison (dotted).
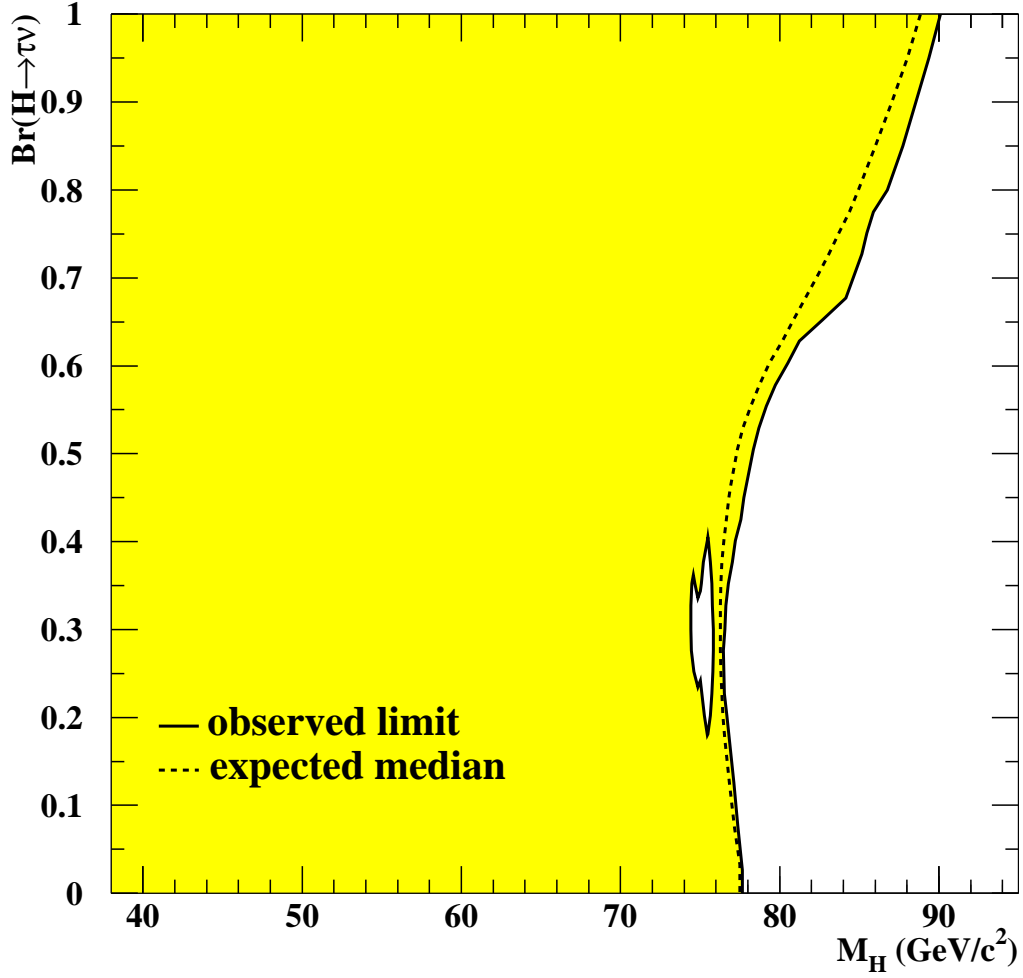
Figure 13: The observed and expected exclusion regions at 95% confidence level in the plane of BR($H^- \to \tau^- \bar{\nu}_\tau$) vs. M$_H$. These limits were obtained from a combination of the search results in the $\tau^+ \nu_\tau \tau^- \bar{\nu}_\tau$, c$\bar{s}\tau^- \bar{\nu}_\tau$ and c$\bar{s}$c$\bar{s}$ channels at $\sqrt{s} = 189$–209 GeV, under the assumption that the W$^*A$ decay is forbidden.
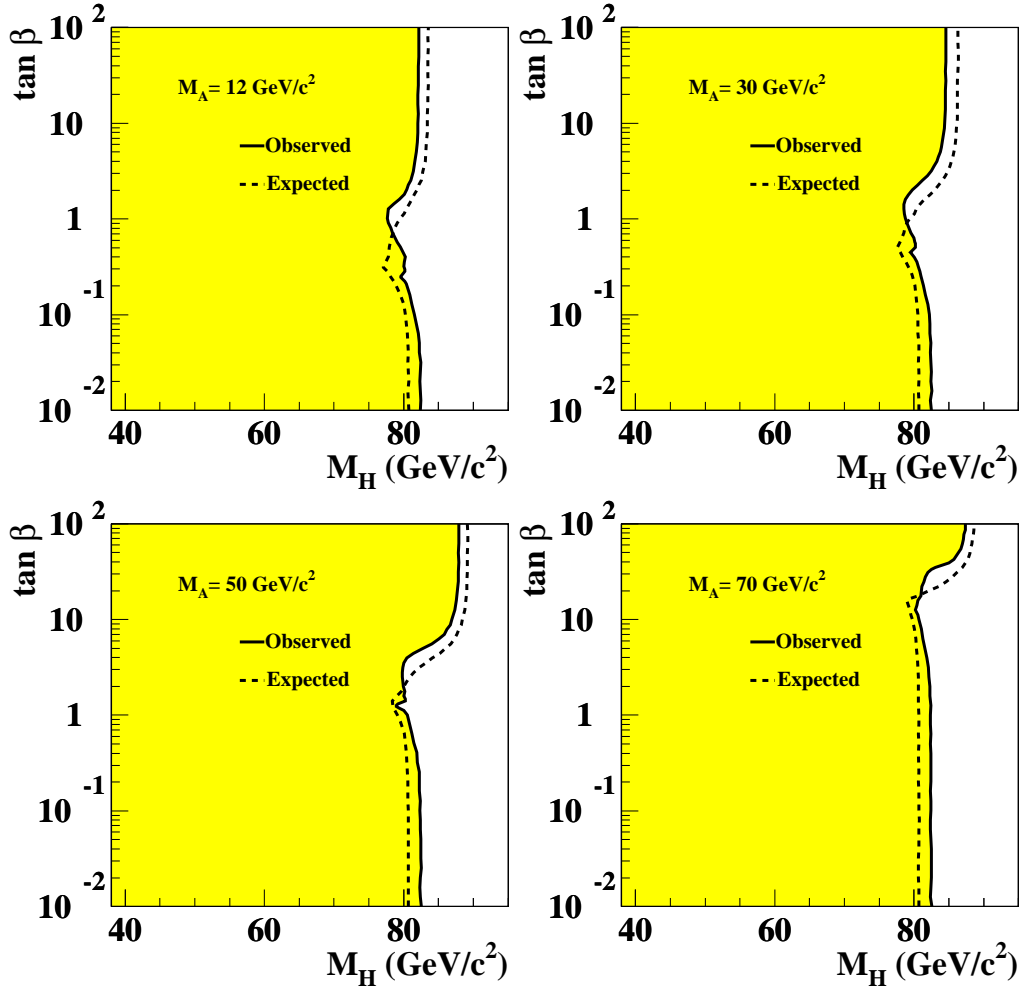
Figure 14: The observed and expected exclusion regions at 95% confidence level in the plane of $\tan\beta$ vs. M_H in the framework of type I Two Higgs Doublet Models. These limits were obtained from a combination of the search results in all studied channels, with or without W^*A decays, at $\sqrt{s} = 189\text{--}209$ GeV, for different A masses.
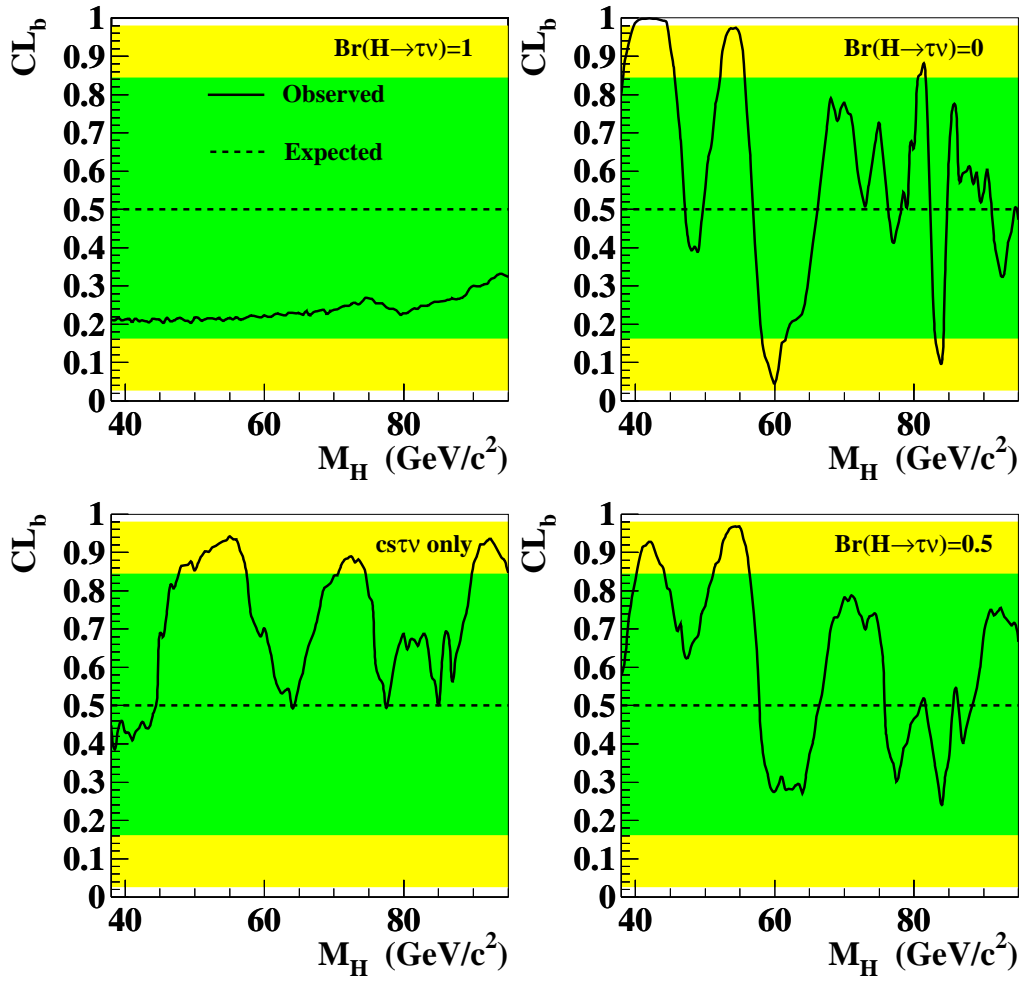
DELPHI
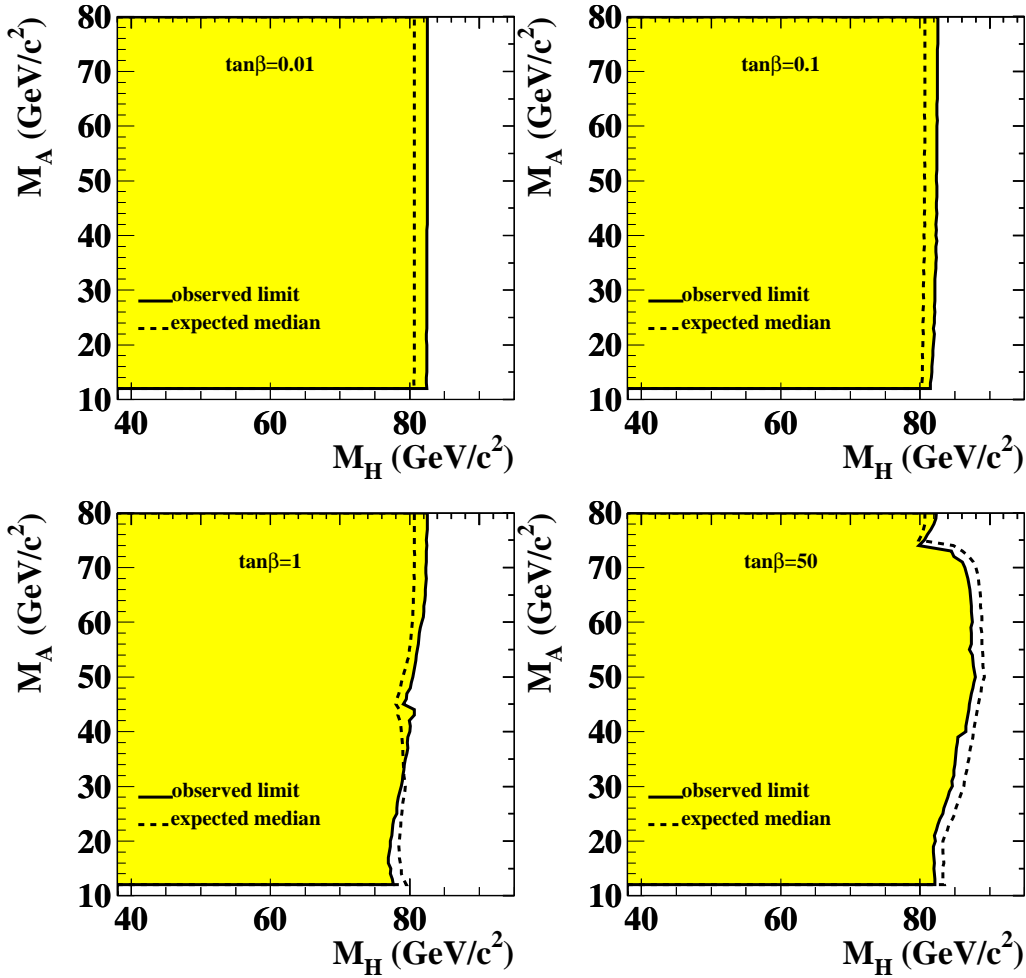
Figure 15: The observed and expected exclusion regions at 95% confidence level in the plane of M_A vs. M_H in the framework of type I Two Higgs Doublet Models. These limits were obtained from a combination of the search results in all studied channels, with or without W^*A decays, at $\sqrt{s} = 189$–209 GeV, for different values of $\tan\beta$.

Figure 16: Confidence level for the background-only hypothesis for different branching ratios, under the assumption that the W$^*A$ decay is forbidden. The bottom left figure, shows the CL_b only for the events selected in the $c\bar{s}\tau^-\bar{\nu}_\tau$. The full line shows the observed CL_b and the horizontal dashed line at 0.5 indicates the expectation in the absence of a signal. The bands show the one and two standard deviation regions for this expectation.
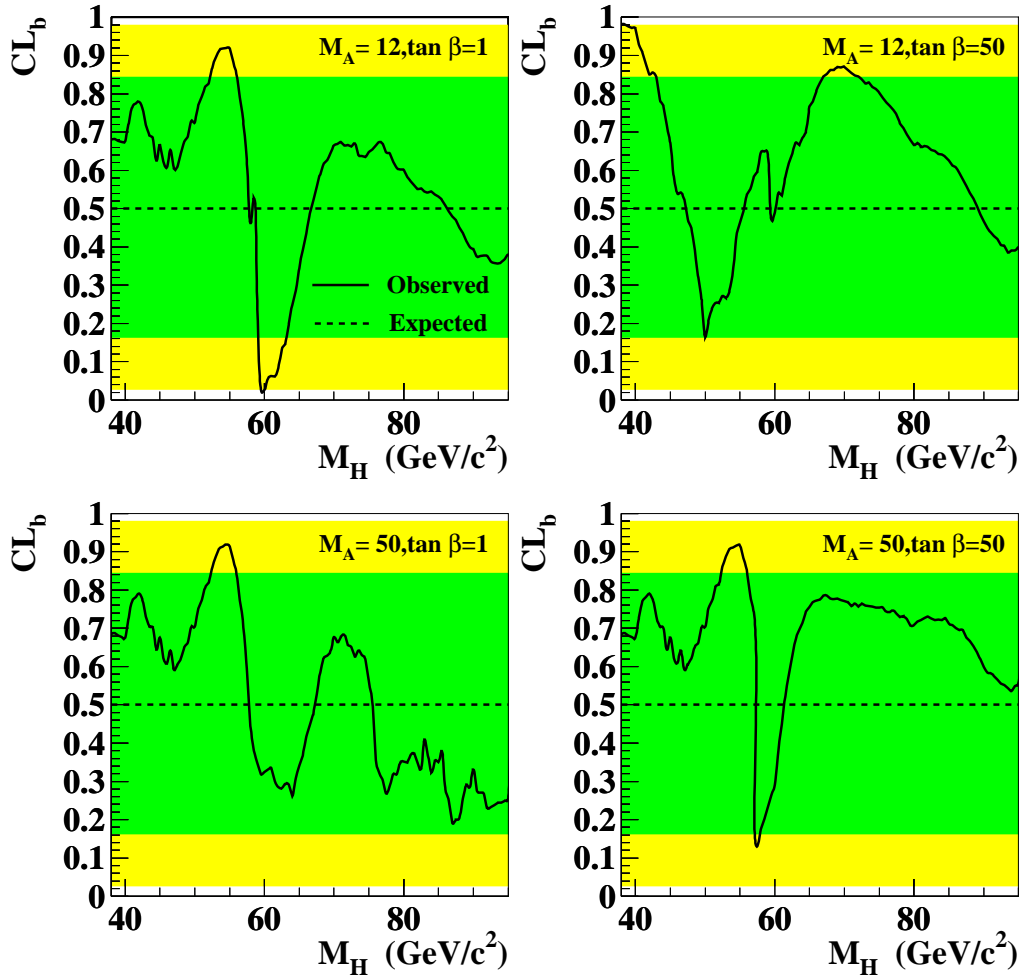
DELPHI

Figure 17: Confidence level for the background-only hypothesis for different $\tan\beta$ and A masses. The full line shows the observed CL_b and the horizontal dashed line at 0.5 indicates the expectation in the absence of a signal. The bands show the one and two standard deviation regions for this expectation.
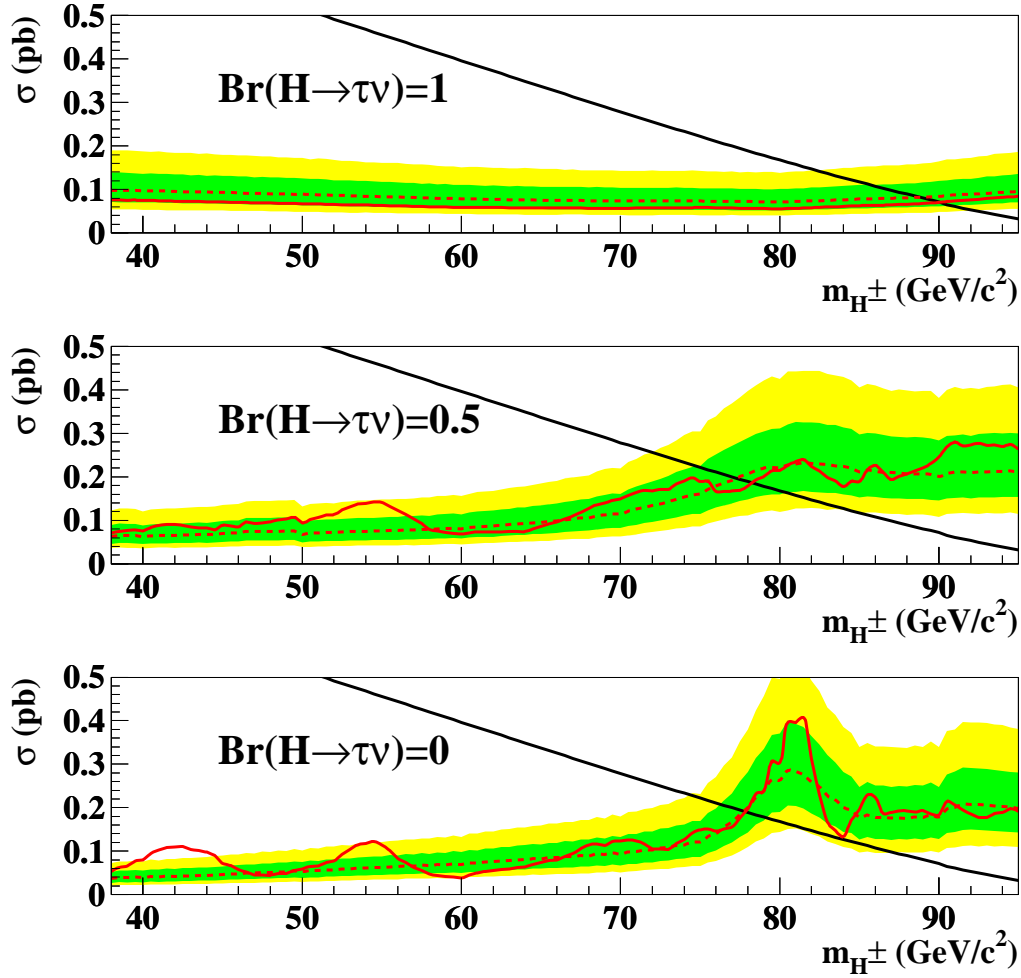
Figure 18: Upper limits on the cross-section for charged Higgs boson pair production at 95% confidence level, for different $BR(H^- \to \tau^- \bar{\nu}_\tau)$, under the assumption that the W^*A decay is forbidden. The dashed curve shows the expected upper limit with one and two standard deviation bands and the solid curve is the observed upper limit of the cross-section for background only hypothesis. The solid black diagonal curve shows the Two Higgs Doublet Model prediction. Cross-sections are given for 206.6 GeV centre-of-mass energy.
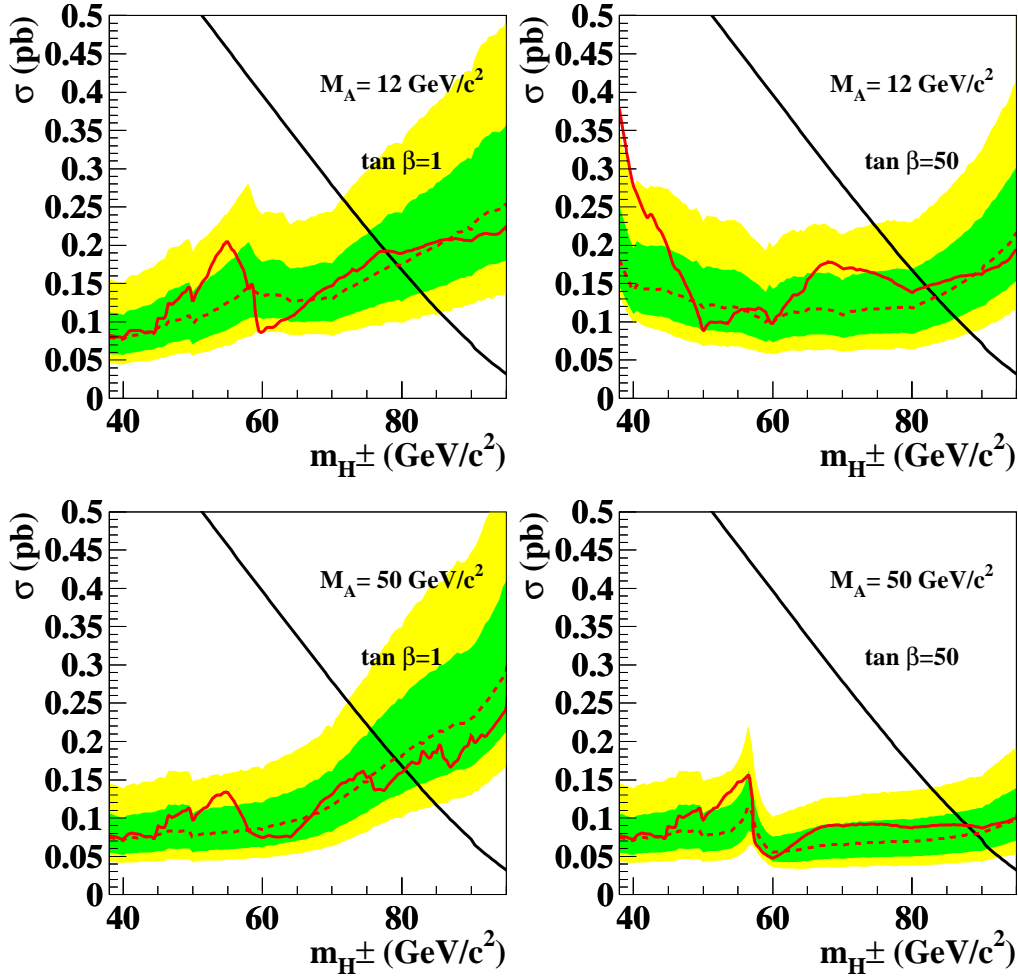
Figure 19: Upper limits, at 95% confidence level, on the production cross-section for a pair of charged Higgs bosons as a function of the charged Higgs boson mass, for different $\tan\beta$ and M_A values within type I models. The dashed curve shows the expected upper limit with one and two standard deviation bands and the solid curve the observed upper limit of the cross-section for background only hypothesis. The solid black diagonal curve shows the Two Higgs Doublet Model prediction. Cross-sections are given for 206.6 GeV centre-of-mass energy.